Results in Engineering 29 (2026) 109380

Contents lists available at ScienceDirect

Results in Engineering

journal homepage: www.sciencedirect.com/journal/results-in-engineering

Research paper

Numerical analysis of magnetohydrodynamic mixed convection for electronic thermal management: Coupling nano-encapsulated PCM with double-diffusive transport

Ahmed M. Hassan [a,*], Mohammed Azeez Alomari [a,b], Mohammad Ghalambaz [c,d], Omaima Jabbar [a], Faris Alqurashi [e], Mujtaba A. Flayyih [f]

[a] Department of Mechanical Engineering, University of Al-Qadisiyah, Al-Qadisiyah, 58001, Iraq
[b] College of Engineering, University of Warith Al-Anbiyaa, Karbala, Iraq
[c] Department of Mathematics, Saveetha School of Engineering, SIMATS, Chennai, India
[d] Laboratory on Convective Heat and Mass Transfer, Tomsk State University, 634050, Tomsk, Russia
[e] Department of Mechanical Engineering, College of Engineering, University of Bisha, Bisha 61922, P.O. Box 551 Saudi Arabia
[f] Biomedical Engineering Department, College of Engineering and Technologies, Al-Mustaqbal University, Hillah, Iraq

ARTICLE INFO

Keywords:
Trapezoidal cavity
Mass transfer
Phase change
NEPCM
Entropy generation

ABSTRACT

This study numerically investigates the hydrothermal performance and entropy generation in a trapezoidal cavity filled with nano-encapsulated phase change material (NEPCM)-water mixture for electronic cooling under magnetohydrodynamic (MHD) and double-diffusive mixed convection. The governing equations were solved using the Galerkin finite element method. The novelty lies in exploring the coupled effects of MHD suppression and NEPCM thermal enhancement on integrated circuit (IC) cooling performance. Key parameters investigated include Reynolds number ($Re = 10 - 100$), Richardson number ($Ri = 0.1 - 7$), Lewis number ($Le = 0.1 - 10$), Hartmann number ($Ha = 5 - 80$), NEPCM volume fraction ($\phi = 0.015 - 0.035$), Stefan number ($Ste = 0.1 - 0.8$), and fusion temperature ($\theta_f = 0.1 - 0.9$). Results reveal that heat transfer enhancement reaches 192.77% at $Re = 100$ when Ri increases from 0.1 to 7, with $Le = 0.5$, $Nz = 2$, $Ste = 0.1$, $\theta_f = 0.5$, $\phi = 0.01$, and $Ha = 10$ held constant), while NEPCM concentration increases the average Nusselt number (Nu_{av}) by 33.77% when ϕ increases from 0.015 to 0.035 at $Re = 50$, $Ri = 1$, $Le = 0.5$, $Nz = 2$, $Ste = 0.1$, $\theta\_f = 0.5$, *and* $Ha = 10$. However, magnetic field strength suppresses convection, reducing heat transfer. Mass transfer characteristics show strong Lewis number sensitivity but remain insensitive to phase change parameters. Entropy generation decreases with both NEPCM concentration and magnetic field strength. These findings provide optimization guidelines for designing energy-efficient electronic cooling systems utilizing NEPCM under magnetic field influence.

1. Introduction

There is considerable interest in mixed convection, which is a phynominan in which free convection occurs simultaneously with forced convection [1–4]. The most commonly used applications of mixed convection are thermal management systems [5,6], cooling solutions for electronic devices [7–9], the nuclear power industry [10–14], clean power implementations [15–20].

The geometry is very essential in controlling thermal and solutal of mixed convection and hence many geometries have been explored [21–23]. Alsabery et al. [24] used numerical methods to assess how wavy walls impact mixed convection. It was found that the thermal performance as well as the fluid flow were highly dependent on the waves, with the heat performance increasing as the waves increased. An investigation of heat and mass transfer by mix convection has been conducted by Alsabery et al. [25] by using varying interior cylinder sizes. In conclusion, the size of the interior cylinder greatly influences the flow of mass and heat. Another paper studied the effects of using an internal cylinder on the mixed convection double-diffusive [26]. This study confirms the earlier founding that the internal cylinder had very effective role in controlling the transfer of heat and mass. Another

* Corresponding author.
E-mail addresses: ahmed.mohammed.hassan@qu.edu.iq (A.M. Hassan), mohammed.hasan@qu.edu.iq (M.A. Alomari), mghalambaz@gmail.com (M. Ghalambaz), Omaimajabar@qu.edu.iq (O. Jabbar), fars421@hotmail.com (F. Alqurashi), mujtaba_abdulkadhim@uomus.edu.iq (M.A. Flayyih).

https://doi.org/10.1016/j.rineng.2026.109380
Received 23 July 2025; Received in revised form 14 January 2026; Accepted 30 January 2026
Available online 31 January 2026

Nomenclature

B_o	Magnetic field strength ($A.\ m^{-1}$)
Be	Bejan number
c, C	Dimensional concentration and Dimensionless concentration
C_p	Constant pressure specific heat ($J.\ kg^{-1}.K^{-1}$)
Cr	The heat capacity ratio (suspension/base fluid)
$\mathfrak{D}$	Coefficient of mass diffusivity ($m^2.s^{-1}$)
g	Gravity constant ($m.s^{-2}$)
Ha	Hartmann number
k	Thermal conductivity ($W.m^{-1}.K^{-1}$)
Le	Lewis number
n	Normal direction to the wall
Nc	The number of thermal conductivity for the suspension
Nu	Nusselt number
Nv	The number of dynamic viscosity for the suspension
Nz	buoyancy ratio parameter
p, P	Dimensional pressure (Pa) and Dimensionless pressure
Pr	Prandtl number
Ra	Rayleigh number
Re	Reynolds number
Ri	Richardson number
S	Non-dimensional form of Entropy generation
Sh	Sherwood number
Ste	Stefan number
T	Dimensional temperature field (K)
T_{Mr}	Dimensional melting range (K)
$u,\ U$	Dimensional ($m.s^{-1}$) and non-dimensional x-velocity component
v, V	Dimensional ($m.s^{-1}$) and non-dimensional y-velocity component
W	Width of cavity, the characteristic length
x, X	Dimensional (m) and non-dimensional x-Cartesian coordinate
y, Y	Dimensional (m) and non-dimensional y-Cartesian coordinate

Greek symbols

$\imath$	Core-shell weight ratio
α	Coefficient of thermal diffusivity ($m^2.s^{-1}$)
β_c	Concentration coefficient
β_T	Coefficient of thermal expansion (K^{-1})
δ	Non-dimensional phase change band
ΔT	Dimensional phase change band (K^{-1})
Θ	Temperature field in a non-dimensional form
θ_f	Non-dimensional form of fusion temperature
λ	Heat capacity ratio
μ	Dynamic viscosity ($kg.\ s^{-1}.m^{-1}$)
ν	Kinematic viscosity ($m^2.s^{-1}$)
ρ	Density ($kg.m^{-3}$)
σ	Electrical conductivity ($S.m^{-1}$)
ϕ	Volumetric fraction of the nanoparticle
χ	The irreversibility factor
ψ	Stream-function
Ω	Rotating speed

Subscript

av	Average value
bf	Base fluid
c	Cold wall
co	The core of NEPCM particle
f	Fusion
h	Hot wall
loc	Local value
nf	Nanofluid
p	NEPCM particles
sh	Shell of NEPCM particle
θ	Thermal
ψ	Viscous

Abbreviation

CPU	Central processing unit
MHD	Magnetohydrodynamics
NEPCM	Nano–Encapsulated Phase Change Material

challenging paper was carried out by Li et al. [27] who investigated mix convection by considering multiple cylinders in rotation. The results confirmed that the internal cylinders had very vital role of controlling the transformation of mass and heat.

Improving thermal performance of some systems, like a solar trough collector, can highly improve the overall efficiency of the applications and this aim can be achieved by using high thermal working fluid, i.e. [28–32] nanofluid. There are many types of nanofluids with different shapes which have been explored to achieve the higher performance with lower cost [33–36]. A numerical study conducted by Selimefendigil et al. [37] investigated the effect of changing the shape of silicon dioxide nanoparticles in a cavity with a rotating cylinder was conducted. The authors concluded that the thermal performance was improved by adding nanoparticles, and that their cylindrical design was the most effective shape. Zhang et al. [38] investigated mixed convection in an enclosure containing Ag/water nanofluids. Some of the variables that had been considered were ϕ, Ri and *Re*. The results indicated that nanoparticle addition increased thermal transfer. This improvement further improved upon rising the volume concentration of the nanofluid. Cu/water was considered by Rajarathinam et al. [39] who stated similar finding of adding nanoparticles.

Thermal performance of the phase change material is slightly low; however, it has very high capacity to store heat. Researchers have found a clever way to combine the benefit of using sell nanoparticles, which are mainly made of metal, and filled their cores with phase change material which called NEPCMs (nano encapsulated PCMs) [40–43]. Irshad *et al.* [44] studied convection with double diffusivity in an enclosure containing NEPCMs. Researchers took into account a number of variables including θ_f and the results stated that melting zone was highly influenced by the mentioned parameter while had lower thermal performance impact. A numerical study by Herouz et al. [45] investigated mixed convection inside an octagonal enclosure containing porous NEPCMs. The authors considered range of *Re*, Da, θ_f and ϕ from which the results stated a noticeable improvement in heat transfer with increasing in Da number. Da number. Raizah and Aly [46] numerically studied double-diffusive mix convection within a porous media enclosure with a rotating cylindrical interior. According to the results, cylinder size had a high influence on the thermal and mass transformation and confirmed the previous founds regarding the Da number.

The magnetohydrodynamic has very high influence on heat, mass and fluid flow for that reason this topic has attracted many authors [47–51]. MHD's impact on double diffusive mixed convective flow was studied by Sáchica et al. [52]. The strength of the streams was drop by the presence of the MHD and both transformation for mass and heat were also dropped down. The same indications was stated by Mondal and Mahapatra [53] who investigated how MHD affects double diffusive convective flow. Furthermore, the negative influence of the MHD was heightened as the Ha number increased.

Despite extensive research in this field, several critical gaps remain unaddressed. First, while NEPCM and MHD effects have been studied independently, their synergistic interaction in electronic cooling applications remains poorly understood. Second, the influence of trapezoidal geometry—which better represents realistic electronic enclosure designs—on the coupled thermal-solutal-electromagnetic transport has not been systematically investigated. Third, comprehensive entropy generation analysis under combined NEPCM-MHD effects is lacking, despite its importance for energy-efficient system design. The present study addresses these gaps by investigating the entropy generation and hydrothermal performance of a trapezoidal cavity containing NEPCM-water mixture under magnetic fields and double-diffusive mixed convection for IC cooling applications. The novelty lies in three key aspects: (1) systematic analysis of the competing effects between MHD-induced flow suppression and NEPCM-enhanced thermal performance, (2) comprehensive parametric investigation of phase change characteristics Stefan number and fusion temperature coupled with electromagnetic and buoyancy-driven transport, and (3) detailed entropy generation analysis to identify optimal operating conditions that balance cooling effectiveness with thermodynamic efficiency. Key parameters evaluated include Reynolds, Richardson, Lewis, Hartmann, and Stefan numbers, along with buoyancy ratio, fusion temperature, and NEPCM volume fraction. This study provides valuable guidelines for optimizing electronic cooling systems by providing a comprehensive understanding of the interactions between forced convection, natural convection, magnetic damping, and phase change phenomena. Special attention is given to entropy generation analysis, which is crucial for designing energy-efficient thermal management solutions that minimize irreversibilities while maximizing heat dissipation from IC components.

2. Modeling mathematics

The physical representation shown in Fig. 1, consists of a trapezoidal cavity containing a mixture of water and NEPCMs (Nano-Encapsulated PCMs), subjected to horizontal magnetic fields (B_o). The cavity functions as a cooling system for four integrated circuits (ICs) positioned along the cavity walls, with dimensions of 0.2 $W \times$ 0.2 W each. The geometric configuration is characterized by a base width (W), a top width (1.5 W), and a height (W), as detailed in Fig. (1). The ICs generate heat, maintaining temperatures and concentrations of (T_h) and (C_h), respectively. The upper surface remains at a lower degree of heating (T_c) and concentration (C_c), with thermally insulated inclined walls.

The system employs double-diffusive mixed convection, with the water-NEPCMs mixture serving as a working fluid. The NEPCM particles consist of n-Nonadecane core material encapsulated within a polyurethane shell, with their thermophysical properties listed in Table (1) along with other materials used in this investigation [54,55].

The numerical analysis encompasses steady-state laminar flow in two dimensions under combined convection. The Boussinesq approximation is employed to account for density considered negligible. According to such assumptions, incorporating magnetohydrodynamic effects, the set of governing equations can be formulated as follows

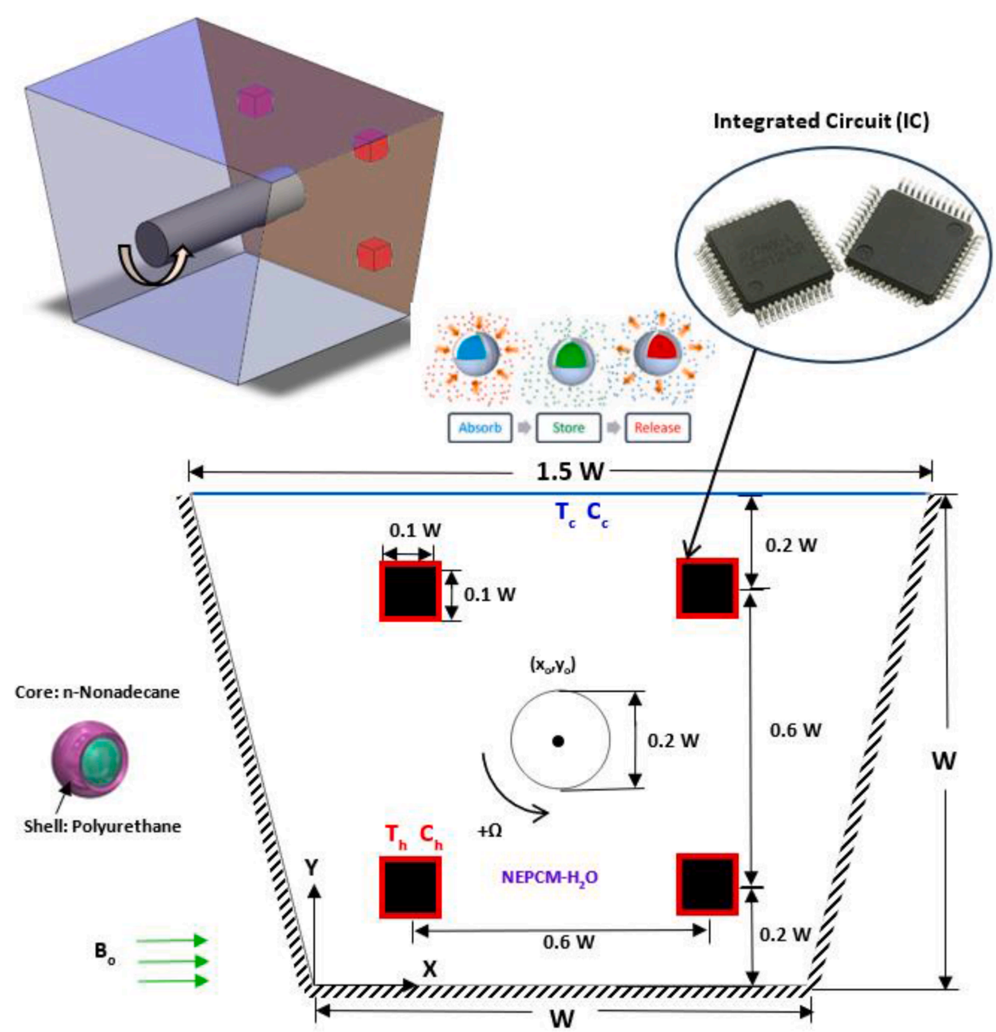

Fig. 1. Detailed physical model.

Table 1
Water and nanoparticles properties at 30 °C [54,55].

Property	Polyurethane Shell	n-nonadecane Core	Water
Density $(kg.m^{-3})$	721	786	996
Dynamic viscosity $(kg.m^{-1}.s^{-1})$	-	-	797×10^{-6}
Specific heat capacity $(J.kg^{-1}.K^{-1})$	2037	1317	4200
Thermal conductivity $(W.m^{-1}.K^{-1})$	0.0253	0.189	0.62
Thermal expansion coefficient (K^{-1})	1.7×10^{-4}	5×10^{-4}	2.1×10^{-4}
The core-to-shell mass ratio (l)	0.45		

[56–58]:

$$\frac{\partial v}{\partial y}+\frac{\partial u}{\partial x}=0 \tag{1}$$

$$v\frac{\partial u}{\partial y}+u\frac{\partial u}{\partial x}=-\frac{1}{\rho_{nf}}\frac{\partial u}{\partial x}+\nu_{nf}\left(\frac{\partial^2 u}{\partial x^2}+\frac{\partial^2 u}{\partial y^2}\right) \tag{2}$$

$$u\frac{\partial v}{\partial x}+v\frac{\partial v}{\partial y}=-\frac{1}{\rho_{nf}}\frac{\partial p}{\partial y}+\nu_{nf}\left(\frac{\partial^2 v}{\partial x^2}+\frac{\partial^2 v}{\partial y^2}\right)+g\frac{(\rho\beta_T)_{nf}}{\rho_{nf}}(T-T_C)+g\frac{(\rho\beta_c)_{nf}}{\rho_{nf}}(c-c_C)-\frac{\sigma_{nf}B_o^2}{\rho_{nf}}v \tag{3}$$

$$(\rho C_p)_{nf}\left(u\frac{\partial T_{nf}}{\partial x}+v\frac{\partial T_{nf}}{\partial y}\right)=k_{nf}\left(\frac{\partial^2 T_{nf}}{\partial x^2}+\frac{\partial^2 T_{nf}}{\partial y^2}\right) \tag{4}$$

$$u\frac{\partial c}{\partial x}+v\frac{\partial c}{\partial y}=\mathfrak{D}_{bf}\left(\frac{\partial^2 c}{\partial x^2}+\frac{\partial^2 c}{\partial y^2}\right) \tag{5}$$

In these equations, the variables represent fundamental flow characteristics: v, u are the velocity components along the y and x directions, c is concentration, p is pressure, B_o is magnetic field strength and T denotes temperature. For the NEPCM-water mixture, several thermophysical properties are crucial: density (ρ_{nf}), kinematic viscosity (ν_{nf}), thermal and mass expansion coefficients (β_T, β_c), electrical conductivity (σ_{nf}), thermal conduction factor (k_{nf}), heat specific capacity (C_p), and mass diffusion rate ($\mathfrak{D}_{bf}$). To facilitate numerical analysis, the following formulas are used to convert the governing equations to dimensionless form:

Spatial and Flow Parameters:

Spatial and Flow Parameters:

$$\left.\begin{array}{lll}\text{Normalizedcoordinates} & \frac{y}{W}=Y,\ \frac{x}{W}=X \\ \text{Normalizedvelocities}: & V=\left(\frac{v}{r\Omega}\right), U=\left(\frac{u}{r\Omega}\right) \\ \text{Dimensionlesspressure}: & P=\frac{p}{\rho_{bf}\, r^2\Omega^2} \\ \text{Normalizedtemperature}: & \theta=\frac{T-T_c}{T_h-T_c} \\ \text{Normalizedconcentration}: & C=\frac{c-c_c}{c_h-c_c}\end{array}\right\} \tag{6}$$

NEPCM-Mixture Properties:

$$\left.\begin{array}{ll}\text{Relativeviscosity}: & \frac{\mu_{nf}}{\mu_{bf}}=(1+N_v.\phi) \\ \text{Relativethermalconductivity}: & \frac{k_{nf}}{\mu_{bf}}=(1+N_c.\phi) \\ \text{Double}-\text{diffusiveparameter}: & Nz=\frac{\beta_c(c_h-c_c)}{\beta_T(T_{nf}-T_c)}\end{array}\right\} \tag{7}$$

Characteristic Dimensionless Numbers:

$$\left.\begin{array}{ll}\text{Lewisnumber}: & Le=\alpha_{bf}/D_{bf} \\ \text{Hartmannnumber}: & Ha=B_o\,W\sqrt{\frac{\sigma_{nf}}{\rho_{bf}\,\nu_{bf}}} \\ \text{Reynoldsnumber}: & Re=\frac{r\Omega L}{\nu_{bf}} \\ \text{Prandtlnumber}: & Pr=\nu_{bf}/\alpha_{bf} \\ \text{Grashofnumber}: & Gr=\frac{g\beta_{bf}\,\Delta TW^3}{\nu_{bf}^2} \\ \text{Rayleighnumber}: & Ra=\frac{g\beta_{bf}\,\Delta TW^3}{\nu_{bf}\,\alpha_{bf}} \\ \text{Richardsonnumber}: & Ri=\frac{Gr}{Re^2}\end{array}\right\} \tag{8}$$

Using these dimensionless parameters, equations (1) through (5) can be transformed into their non-dimensional counterparts, as presented in subsequent equations [5,59].

$$\frac{\partial U}{\partial X}+\frac{\partial V}{\partial Y}=0 \tag{9}$$

$$\left(\frac{\rho_{nf}}{\rho_{bf}}\right)\left(U\frac{\partial U}{\partial X}+V\frac{\partial U}{\partial Y}\right)=-\frac{\partial P}{\partial X}+\frac{1}{Re}\left(\frac{\mu_{nf}}{\mu_{bf}}\right)\left(\frac{\partial^2 U}{\partial X^2}+\frac{\partial^2 U}{\partial Y^2}\right) \tag{10}$$

$$\left(\frac{\rho_{nf}}{\rho_{bf}}\right)\left(V\frac{\partial V}{\partial Y}+U\frac{\partial V}{\partial X}\right)=-\frac{\partial P}{\partial Y}+\frac{1}{Re}\left(\frac{\mu_{nf}}{\mu_{bf}}\right)\left(\frac{\partial^2 V}{\partial X^2}+\frac{\partial^2 V}{\partial Y^2}\right)+\frac{Gr}{Re^2}\left(\frac{(\rho\beta)_{nf}}{\rho_{bf}\beta_{bf}}\right)(\Theta+Nz.C)-\frac{Ha^2}{Re}.V \tag{11}$$

$$\left(U\frac{\partial}{\partial X}(\mathrm{Cr}\ \Theta)+V\frac{\partial}{\partial Y}(\mathrm{Cr}^*)\right)=\frac{1}{Re.Pr}\left(\frac{k_{nf}}{k_{bf}}\right)\left(\frac{\partial^2\Theta}{\partial X^2}+\frac{\partial^2\Theta}{\partial Y^2}\right) \tag{12}$$

$$\mathrm{U}\frac{\partial \mathrm{C}}{\partial \mathrm{X}}+V\ \frac{\partial \mathrm{C}}{\partial \mathrm{Y}}=\frac{1}{Le.\ Re.Pr}\left(\frac{\partial^2\mathrm{C}}{\partial \mathrm{X}^2}+\frac{\partial^2\mathrm{C}}{\partial \mathrm{Y}^2}\right) \tag{13}$$

NEPCM and water are characterized by the following thermophysical properties:

Density Relations:

Nanofluid mixtures have the following effective density:

$$\rho_{nf}=(1-\phi)\rho_{bf}+\phi\rho_p \tag{14}$$

The NEPCM particle density is determined by:

$$\rho_p=\frac{(1+l)\rho_{co}\rho_{sh}}{\rho_{sh}+l\rho_{co}} \tag{15}$$

where the subscripts denote: *bf* (base fluid), *p* (NEPCM particle), *co* (core material), and sh (shell material). In this investigation, the core-to-shell mass ratio (l) is maintained at 0.45 [60].

Thermal Properties:

Using [60], we can determine the nanofluid's specific heat capacity and thermodynamic expansion coefficient:

$$C_{p,nf}=\frac{(1-\phi)(\rho\ C_p)_{bf}+\phi(\rho\ C_p)_p}{\rho_{nf}} \tag{16}$$

$$\beta_{nf} = (1-\phi)\beta_{bf} + \phi\beta_p \tag{17}$$

Based on the phase change effects incorporated into the NEPCM particles, its specific heat capacity can be calculated as follows [61]:

$$C_{p,p} = C_{p,p} + \left\{\frac{\pi}{2}\cdot\left(\frac{h_{sf}}{T_{Mr}} - C_{p,co}\right).\sin\left(\pi\frac{T-T_0}{T_{Mr}}\right)\right\}.\sigma \tag{18}$$

where σ is defined by the temperature-dependent function:

$$\sigma = \begin{cases} 0 \; T > T_0 \\ 1 \; T_1 < \; T < T_1 \\ 0 \; T > T_1 \end{cases} \tag{19}$$

Here, h_{sf} represents latent heat of the core, and T_{Mr} denotes range of temperature of phase change.

Heat Capacity Ratio:

The effective heat capacity ratio is defined as [61]:

$$Cr = \frac{(\rho C_p)_{nf}}{(\rho C_p)_{bf}} = (1-\phi) + \phi\lambda + \frac{\phi}{\delta Ste}f, \tag{20}$$

in which f is [62]:

$$f = \frac{\pi}{2}\sin\left(\frac{\pi}{\delta}\left(\theta - \theta_{fu} + \delta/2\right)\right)\zeta \tag{21}$$

$$\zeta = \begin{cases} 0 & \theta < \theta_{fu} - \delta/2 \\ 1 & \theta_{fu} - \delta/2 < \theta < \theta_{fu} + \delta/2 \\ 0 & \theta > \theta_{fu} + \delta/2 \end{cases} \Bigg| \; \theta_{fu} = \frac{T_{fu} - T_c}{\Delta T}, \tag{22}$$

Dimensionless Parameters:

The key dimensionless parameters characterizing the system are:

Stefan number: $Ste = \frac{(\rho C_p)_{bf}\Delta T(\rho_{sh} + \iota\rho_{co})}{\alpha_{bf}(h_{sf}\rho_{co}\rho_{sh})}$

Melting range: $\delta = \frac{T_{Mr}}{\Delta T}$

Heat capacity ratio: $\lambda = \frac{\rho_{co}\rho_{sh}(C_{p,co} + \iota C_{p,sh})}{(\rho C_p)_{bf}(\rho_{sh} + \iota\rho_{co})}$

Mass and Thermal Transfer Characterization:

Sherwood and Nusselt numbers can quantify mass and thermal transport phenomena. At the upper surfaces, these measurements can be defined as:

$$Nu_{loc} = -(1 + Nc\,\phi)\,\frac{\partial\,\theta_{nf}}{\partial n} \tag{23}$$

$$Sh_{loc} = -(\frac{\partial\, C}{\partial n} \tag{24}$$

The surface-averaged transport numbers are calculated by:

$$Nu_{av} = \frac{1}{s}\int_0^s Nu_{loc}ds \tag{25}$$

$$Sh_{av} = \frac{1}{s}\int_0^s Sh_{loc}ds \tag{26}$$

The flow pattern within the trapezoidal cavity is characterized by streamline contours, defined through:

$$U = \frac{\partial\psi}{\partial Y}, V = -\frac{\partial\psi}{\partial X} \tag{27}$$

The stream function satisfies:

$$\frac{\partial^2\psi}{\partial X^2} + \frac{\partial^2\psi}{\partial Y^2} = \frac{\partial U}{\partial Y} - \frac{\partial V}{\partial X} \tag{28}$$

The total entropy generation comprises thermal and viscous contributions:

$$S_{total} = S_\theta + S_\psi = (1 + Nc\phi)\left[\left(\frac{\partial\theta}{\partial X}\right)^2 + \left(\frac{\partial\theta}{\partial Y}\right)^2\right] + \chi(1 + Nv\phi)\left(2\left(\frac{\partial U}{\partial X}\right)^2 + 2\left(\frac{\partial V}{\partial Y}\right)^2 + \left(\frac{\partial V}{\partial X} + \frac{\partial U}{\partial Y}\right)^2\right) \tag{29}$$

here, the irreversibility factor χ is:

$$\chi = \frac{\mu_{bf}T_0}{k_{bf}}\left(\frac{\alpha_f}{W\,(T_h - T_c)}\right)^2 \tag{30}$$

This is the Bejan number, which represents the ratio between thermal and total entropy production:

$$Be = \frac{S_\theta}{S_{total}} \tag{31}$$

Defining the conditions of the boundaries:

The physical boundary conditions are established based on realistic electronic cooling scenarios. The trapezoidal cavity walls are thermally insulated (adiabatic) to minimize heat loss to the environment, representing typical electronic enclosures designed to direct thermal energy toward designated cooling surfaces. The upper surface is maintained at a constant low temperature (T_c) and concentration (c_c), simulating a heat sink or cold plate that extracts heat from the system. The integrated circuit surfaces are maintained at elevated temperature (T_h) and concentration (c_h), representing active heat-generating components. A rotating cylinder with angular velocity Ω provides mechanical mixing to enhance convective transport, while remaining thermally insulated to function purely as a flow enhancement device.

Following are the dimensionless boundary requirements with physical justifications for electronic cooling applications:

For trapezoidal cavity walls (adiabatic):

$$U = 0,\; V = 0, \frac{\partial\theta}{\partial n} = 0, \frac{\partial C}{\partial n} = 0 \tag{32}$$

These conditions represent thermally insulated enclosure walls, typical in electronic cooling systems where the housing is designed to minimize heat loss to the environment and direct heat flow toward designated cooling surfaces.

At upper surface (cold wall):

$$U = 0,\; V = 0,\; \theta = 0,\; C = 0 \tag{33}$$

This boundary represents a heat sink or cold plate mounted on top of the electronic enclosure, maintained at a reference low temperature (T_c) to extract heat from the system. The zero-concentration condition simulates fresh coolant supply or contaminant-free interface.

At IC surfaces (hot walls):

$$U = 0,\; V = 0,\; \theta = 1,\; C = 1 \tag{34}$$

These conditions model the heat-generating integrated circuits operating at elevated temperature (T_h) with high solute concentration, representing thermal and species sources typical of active electronic components during operation.

At the rotating cylinder surface (adiabatic):

$$U = -\Omega\,(Y - Y_o),\; V = \Omega\,(X - X_o),\; \frac{\partial\theta}{\partial n} = 0,\; \frac{\partial C}{\partial n} = 0 \tag{35}$$

The rotating cylinder serves as a mechanical mixer to enhance convective heat transfer within the NEPCM-water mixture, simulating active cooling enhancement mechanisms such as rotating fans or impellers commonly used in electronic thermal management systems. The adiabatic thermal condition ensures that the cylinder functions purely as a flow mixing device without adding or removing heat from the system.

These equations give a comprehensive mathematical model of entropy generation, heat transfer, and fluid flow in an NEPCM-filled trapezoidal cavity with integrated circuits for practical electronic cooling applications

3. Setting up and validating the solver

The governing equations (Eqs. (6)–10) have been solved numerically using Galerkin weighted finite elements approach implemented in COMSOL Multiphysics 6.2. An unstructured mesh is used to discretize the computation domain with refined elements near the IC surfaces and cavity boundaries, as illustrated in Fig. (2, a). The discretized equations are solved using a damped Newton method for robust coupling, while the resulting linear system is handled by a Parallel Sparse Direct Solver.

The numerical solution is considered converging if the residuals of each variable (V, U, θ, C and P) reach a threshold of 10^{-5}. To ensure

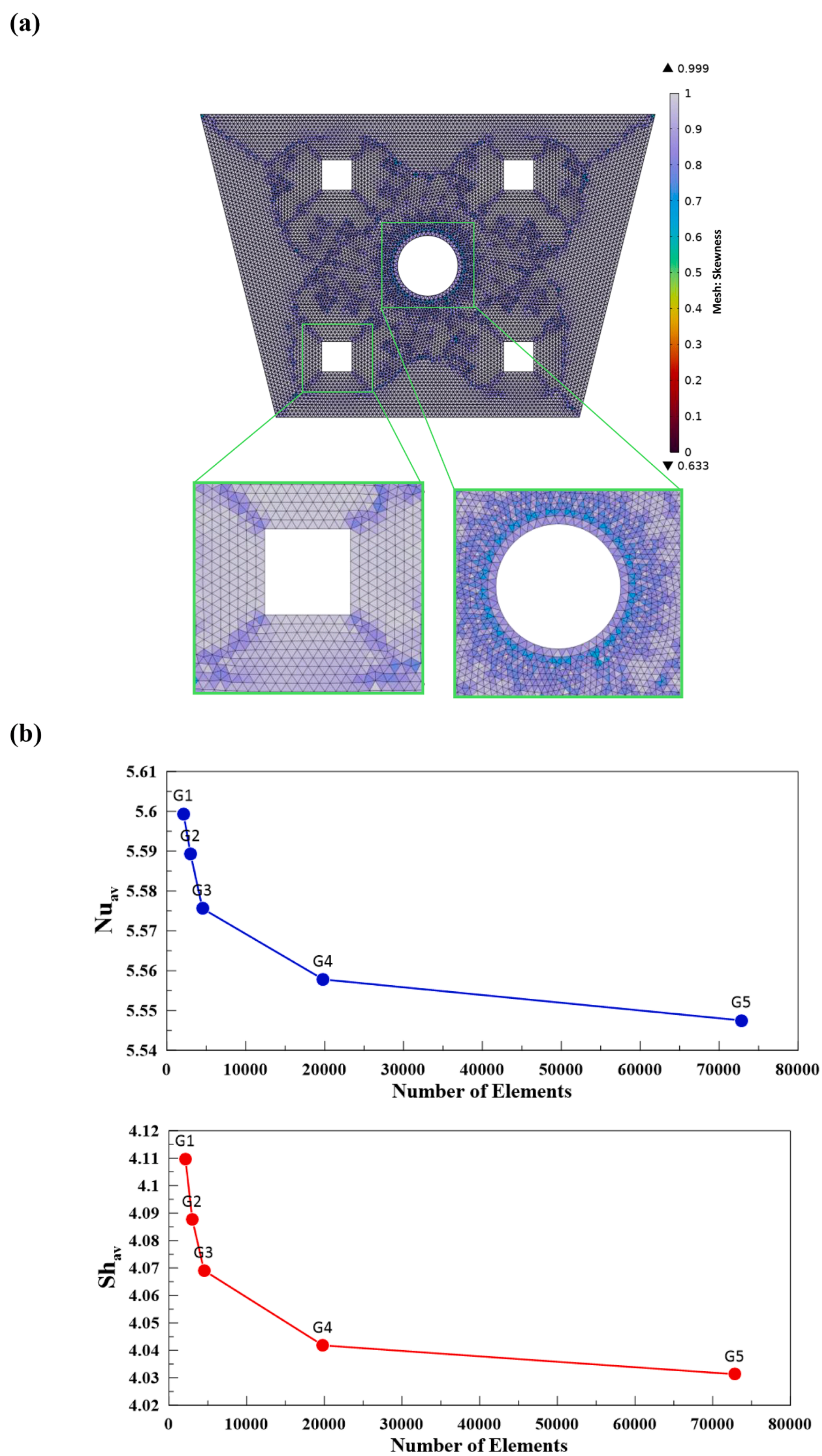

Fig. 2. (a) Grid distrbution, (b) Grid independence results.

solution stability, extended iterations were performed beyond the convergence point, confirming that variations in key parameters remained below 0.01 %. The computational analysis was performed using COMSOL Multiphysics 6.2.

A comprehensive grid independence analysis was performed using five distinct mesh configurations, ranging from 2107 to 72,850 elements. The study was conducted under specific parametric conditions: Reynolds number = 50, Richardson number = 1, Stefan number = 0.1, Lewis number = 0.5, buoyancy ratio = 2, NEPCM volume fraction = 0.01, and phase change temperature (θ_f) = 0.5. Fig. (1 b) illustrates that the mean Nusselt number decreased from 5.5994 to 5.5475, while the average Sherwood number reduced from 4.1098 to 4.0313 as the mesh was refined. The fourth grid configuration, containing 19,823 elements, demonstrated optimal computational efficiency with minimal variation in results compared to the finest mesh, showing relative differences of 0.18 % for Nu_{av} and 0.26 % for Sh_{av}. Therefore, this mesh resolution was adopted for all subsequent numerical simulations in the present study.

The present numerical model underwent multiple validation stages through comparison with established literature. It was first validated by comparing it to the computational results of Rawa et al. [63], that focused on mixed convective heat transfer in NEPCM-water systems. The present and their findings are shown to be very similar in terms of both thermal patterns and magnitudes in Fig. 3.

The numerical methodology was further validated through comparison with the work of Usman et al. [64], who studied free convection with radiation effects in a multi-obstacle cavity configuration. The comparison was performed for specific parameters: Rayleigh number (Ra = 10^4), radiation parameter (Rd = 5), thermal conductivity ratio (λ = 0.5), Lewis number (Le = 10), and buoyancy ratio (Nz = 0.5). Fig. 4 reveals strong agreement in flow characteristics, thermal patterns, and species distribution. The numerical predictions accurately captured the formation of primary vortices, thermal stratification around obstacles, and concentration gradients throughout the domain.

Additional validation was performed against the experimental results of Kuehn and Goldstein [65], as presented in Fig. 5. This comparison specifically examined natural convection around a circular cylinder through isotherm analysis. The numerical predictions showed remarkable consistency when compared to the experimental results, especially in representing heat boundary layer development and temperature field distribution around the cylinder. The close alignment between experimental and numerical results demonstrates the precision and reliability of our present numerical approach to modeling complex convective heat transfer phenomena.

4. Evaluation and discussion of results

The numerical investigation encompasses an in-depth parametric evaluation examining various physical and thermodynamic phenomena in the NEPCM-filled trapezoidal cavity with integrated circuits. The study explores combined convection effects by varying the Richardson number from 0.1 to 10, and the Reynolds number from 10 to 100. Mass transfer characteristics are analyzed through variations in buoyancy

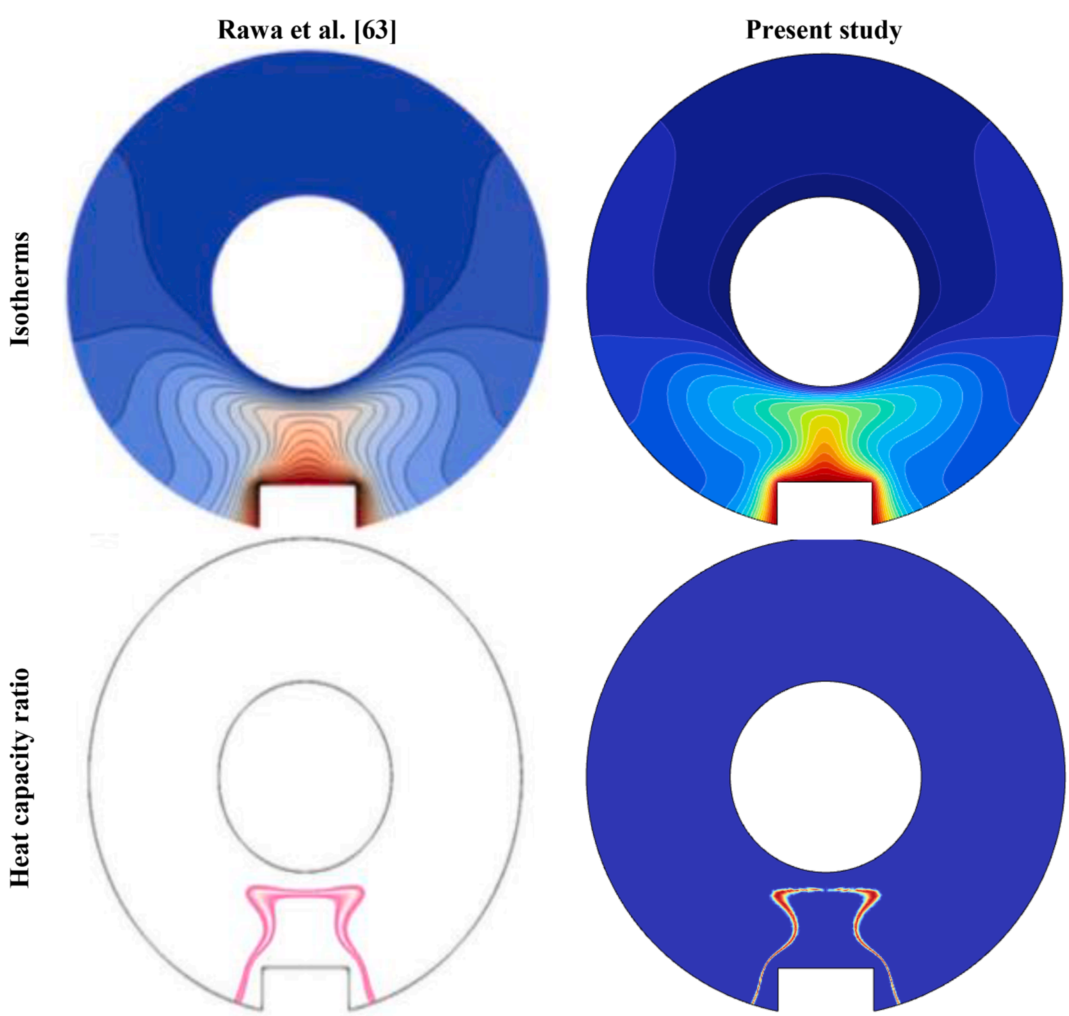

Fig. 3. current outcomes versus Rawa et al. [63].

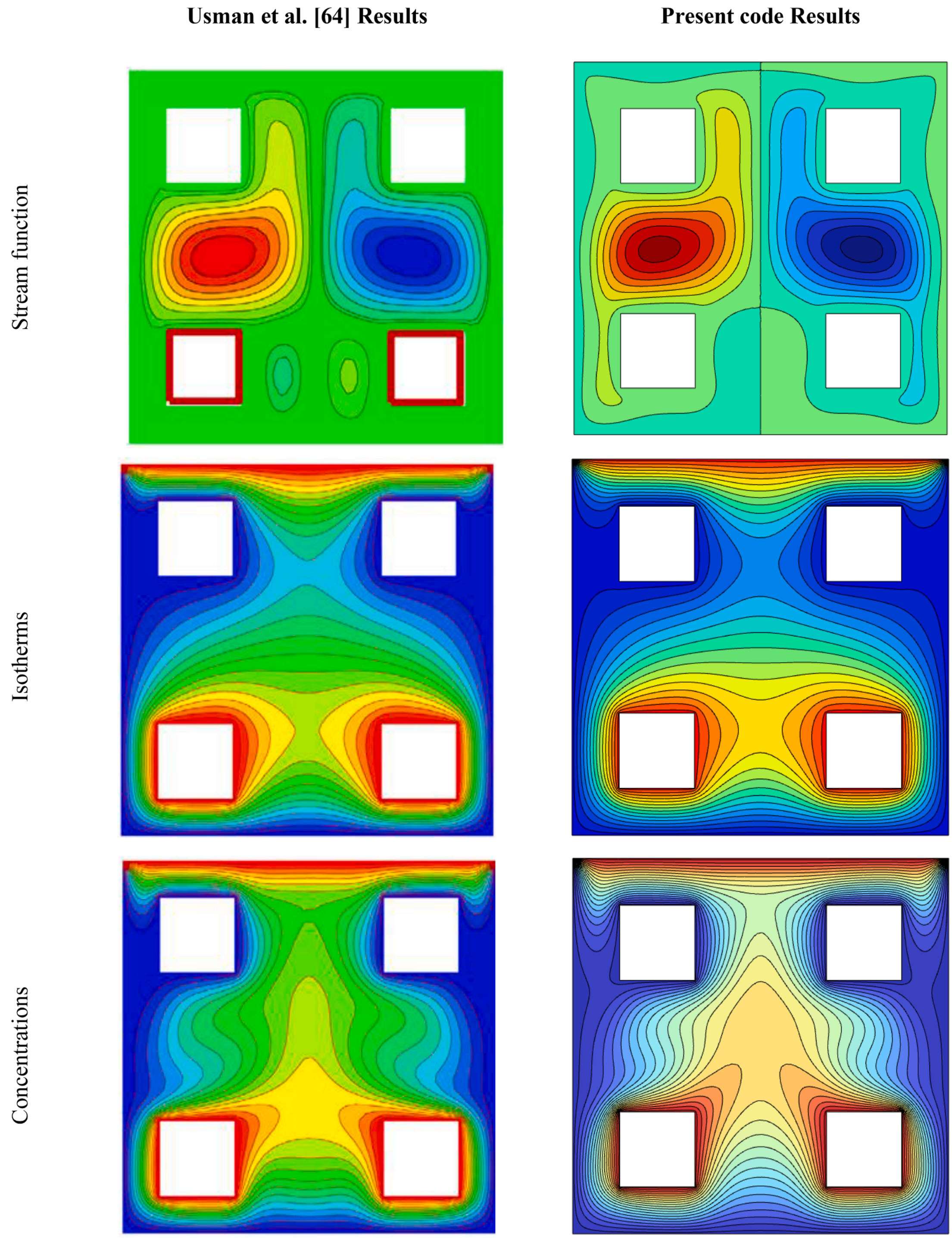

Fig. 4. Comparison of stream function, isotherms, and concentrations with Usman et al. [64] at $Ra = 10^4$, $Rd = 5$, $\lambda = 0.5$, $Le = 10$, and $Nz = 0.5$.

ratios ranging 1–5, and Lewis numbers ranging 0.1–10. The influence of magnetic fields is investigated by modulating the Ha (Hartmann number) between 5 and 80. The NEPCM properties and phase change dynamics are examined by varying the volume fraction between 0.015 and 0.035, Stefan number between 0.1 and 0.8, and fusion temperature between 0.1 and 0.9. Throughout the investigation, certain parameters are maintained constant: Prandtl number is fixed at 6.25, the dynamic viscosity parameter is set at 12.5, and the thermal conduction parameter is fixed at 23.80. The analysis presents temperature distributions, concentration patterns, streamline contours, and specific heat ratio variations within the trapezoidal cavity. Heat and mass transfer performance are quantified through Sherwood number (Sh_{av}) and mean Nusselt (Nu_{av}) number at the IC surfaces. Additionally, the study evaluates the thermodynamic performance through total entropy production and the Bejan numbers, providing insights into system irreversibilities.

Fig. (6) demonstrates the role of Re and Ri in altering the contours of ψ, θ, C and C_r at fixed values of Ha=10, $\phi = 0.01$, Ste = 0.1, $\theta_f = 0.5$, Le = 0.5, Nz =2. At lower Ri values, streamlines concentrate primarily around the rotating cylinder, indicating that forced convection dominates the flow field. This occurs because the mechanical stirring effect of the cylinder overwhelms the relatively weak buoyancy-driven motion. The rotation-induced vortices remain localized near the cylinder, with

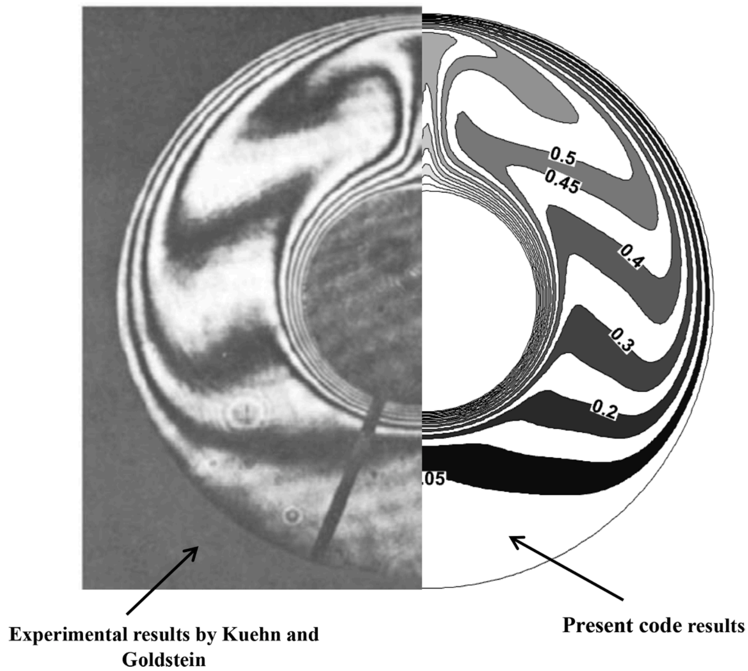

Fig. 5. Isotherm validation between Kuehn and Goldstein's study and the current study[65].

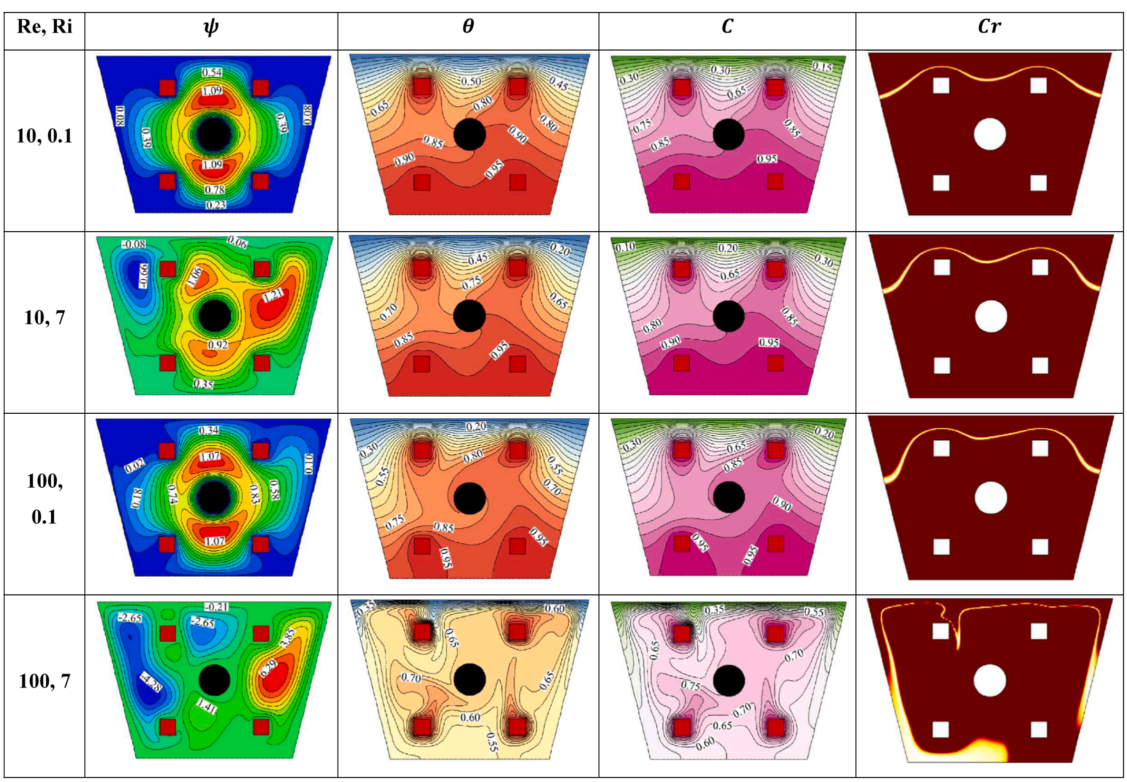

Fig. 6. Contours of ψ, θ, C and Cr with differing Ri & Re at $Ha = 10$, $\phi = 0.01$, $Ste = 0.1$, $\theta_f = 0.5$, $Le = 0.5$, & $Nz = 2$.

limited extension into the bulk fluid. In contrast, at higher (Ri) value(s), the streams are generated away from the cylinder where the influence of the bouncy force becomes stronger than the mechanical stirring effect of the cylinder. This transition reflects the increasing dominance of natural convection, where buoyancy forces drive fluid motion throughout the entire cavity, creating large-scale circulation patterns that extend from the hot IC surfaces to the cold upper wall. Furthermore, the free convective flow becomes dominant as Ri increases, fundamentally altering the transport mechanisms. The value of Ri number does not affect concentrations and isotherms at lower *Re* numbers because weak forced convection results in insufficient mixing to significantly alter temperature and concentration distributions. However, there is a slightly more pronounced effect on both transformations, heat and mass, at higher *Re* values, where enhanced fluid mixing intensifies both thermal and species transport. Moreover, the influence of *Re* on the isotherms and concentrations is very low at lower Ri while the influence of *Re* becomes significant at higher Ri numbers. This synergistic effect occurs because strong buoyancy forces amplify the impact of forced convection, creating more effective heat and mass transfer through combined convective mechanisms. The same behavior is experienced by the melting zone, where this zone is only influenced by the change of *Re* number at higher values of Ri. The melting zone's sensitivity to *Re* at high Ri indicates that effective NEPCM phase change requires sufficient convective intensity to transport thermal energy to the particles, which is achieved only when both forced and natural convection mechanisms work cooperatively.

Fig. (7) demonstrates the role of Nz and Le in altering the contours of ψ, θ, C and Cr at fixed values of *Re*, Ri, Φ, Ha, Ste, and θ_f with the values equal to 50, 1, 0.01, 10, 0.1, and 0.5, respectively. The streams slightly slow down as Le increases with Nz. This deceleration occurs because higher Lewis numbers indicate slower mass diffusion relative to thermal diffusion, which reduces the contribution of solutal buoyancy to the overall flow field. In contrast, streams become stronger with increasing Nz, causing the bouncing force to increase with increasing Nz, causing the streams to circulate away from the cylinder. The enhancement in flow strength with Nz reflects the amplified role of concentration gradients in driving natural convection, as higher buoyancy ratios mean that solutal density variations contribute more significantly to the buoyancy forces. There is, however, a slight difference. On the other hand, the isotherms show very low influence to the change of the Nz and Le and hence these parameters have less impact on the melting region. This insensitivity suggests that the thermal field is primarily controlled by the imposed boundary conditions and flow patterns rather than by the relative magnitudes of thermal and solutal diffusion. On the other hand, Le number significantly affects concentrations, since the latter increases as Le increases regardless of Nz. Higher Lewis numbers correspond to lower mass diffusivity, which reduces the rate at which concentration gradients dissipate, resulting in steeper concentration distributions and stronger stratification near the IC surfaces. In contrast, Nz slightly enhances the strength of the concentrations and this influence is only sensible at higher Le numbers. This coupling effect indicates that when mass diffusion is already slow, the additional solutal buoyancy becomes more effective in redistributing species through convective transport.

Fig. (8) illustrates the role of θ_f in altering the contours of ψ, θ, C and Cr at fixed *Re*, Ri, Le, Nz, Ste, Φ, and Ha at 50, 1, 0.5, 2, 0.1, 0.01, and 10, respectively. It is clear from the contours that θ_f does not affect streams, concentrations, or isotherms. This independence occurs because the fusion temperature determines only when phase change occurs within the NEPCM particles, not the overall flow dynamics or boundary-driven temperature distributions. Conversely, the zone of melting appears to be highly dependent on the θ_f. Low values of θ_f generate melting zones near the low temperature wall, which means that the phase change material inside the nanoparticles requires less temperature to be melted, which means more NEPCMs are engaged. When the fusion temperature is low, a larger portion of the cavity falls within the phase change temperature range, allowing more NEPCM particles to participate in latent heat absorption and thereby enhancing the overall thermal storage capacity of the system. As the θ_f increases, the melting zone moves towards the hot source, indicating that the NEPCMs require higher temperature to be melted and hence less nanolattices are engaged. This shift toward the hot surfaces means that only particles in the high-temperature regions undergo phase change, reducing the effective thermal buffering provided by the NEPCM. At higher θ_f, multiple melting zones are formed near the hot sources, so a relatively low number of NEPCMs becomes active in phase change, concentrating the latent heat absorption in localized regions near the ICs rather than distributing it throughout the cavity.

Fig. (9) demonstrates the role of Ha in altering the contours of ψ, θ, C and Cr at fixed Ri, *Re*, Le, Φ, and Ste at 1, 50, 0.5, 2, 0.01, and 0.1, respectively. At low Hartmann numbers (Ha = 5), there is a strong bouncy force downstream of the rotary cylinder without significant magnetic field suppression. Therefore, free convective flow dominates under these conditions because the streams create two vortices driven by thermal and solutal buoyancy. By increasing the Hartmann (Ha) number, the stream's behaviour changes and becomes more influenced by rotation due to the weakening of the bouncy force. This is due to the Lorentz force, which opposes fluid motion and thereby reduces the

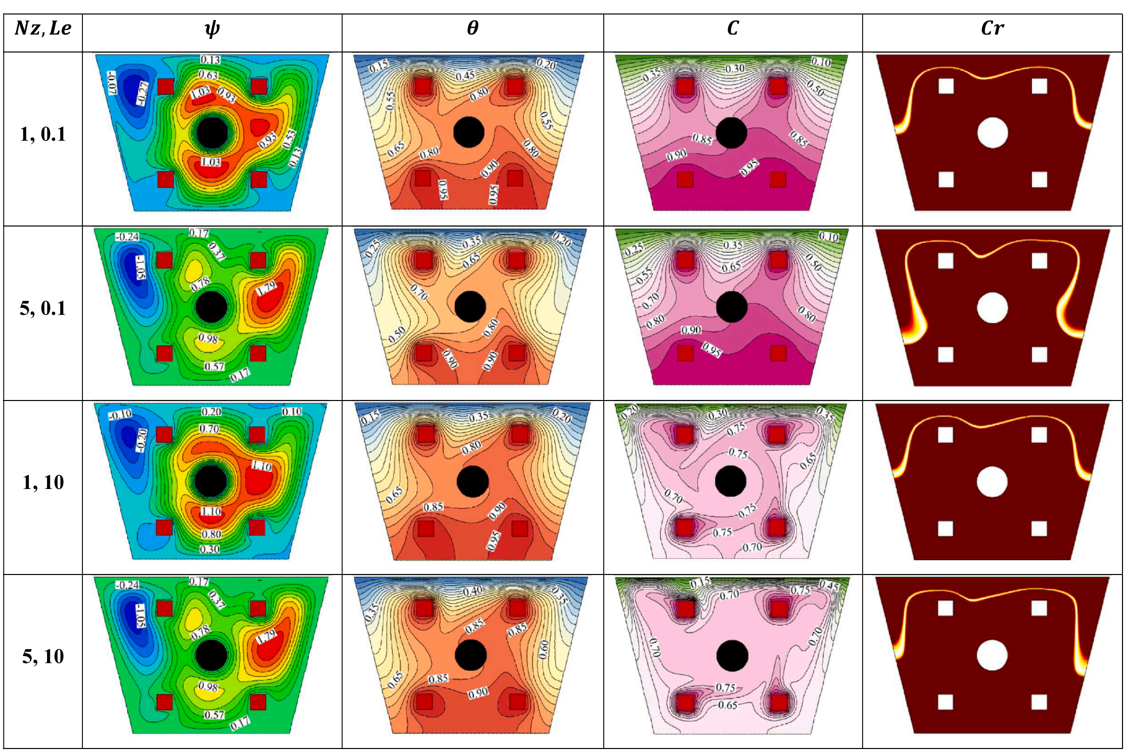

Fig. 7. Contours of $\psi,\ \theta,\ C\ and\ Cr$ based on several *Nz* & *Le* values at $Re = 50$, $Ri = 1$, $\phi = 0.01$, $Ha = 10$, $Ste = 0.1$, and $\theta_f = 0.5$.

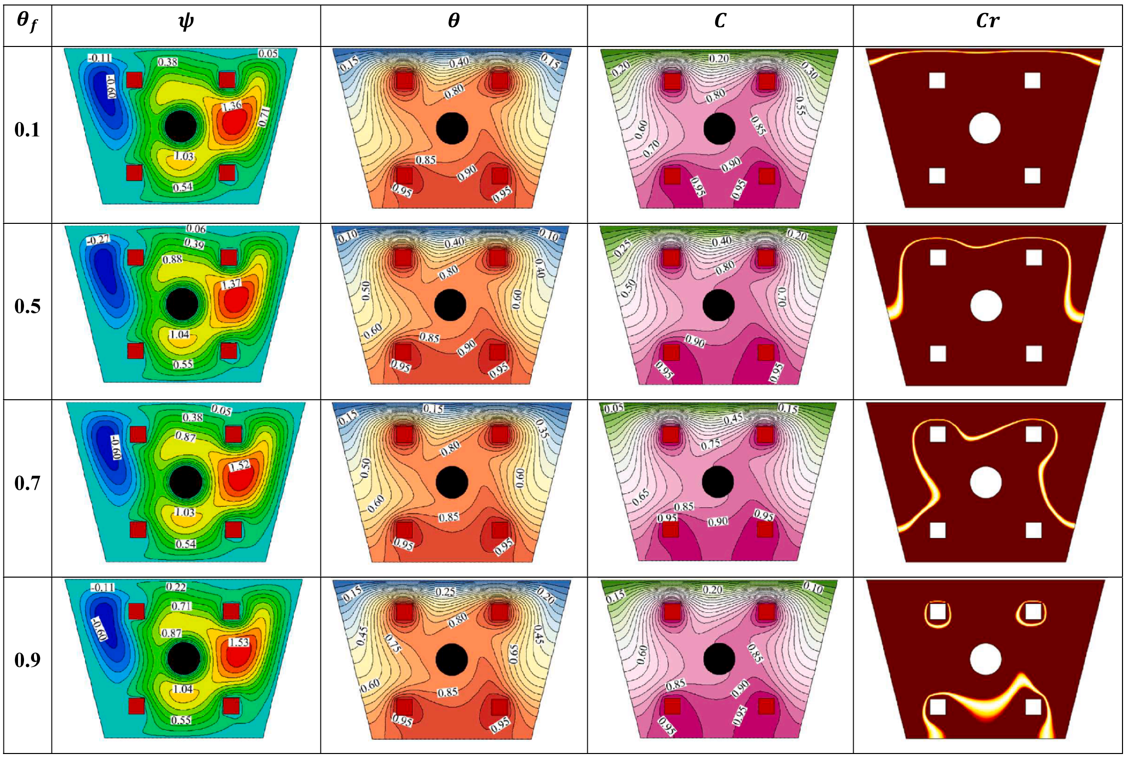

Fig. 8. Contours of ψ, θ, C *and* Cr for different θ_f at $Re = 50$, $Ri = 1$, $Le = 0.5$, $Nz = 2$, $Ste = 0.1$, $\phi = 0.01$, and $Ha = 10$.

bouncy force. The electromagnetic damping effect becomes progressively stronger as Ha increases, suppressing the large-scale circulation patterns and confining fluid motion to regions near the rotating cylinder where mechanical forcing can overcome magnetic resistance. In contrast, the isotherms and concentrations are also decreased with the increase of the Ha due to the less strength of the vortices. Weaker circulation reduces convective transport effectiveness, resulting in more diffusion-dominated heat and mass transfer with steeper gradients near the boundaries and reduced mixing in the bulk fluid. Furthermore, a reduction in the isotherms at the same value of θ_f also affects the melting zone when the Ha number rises. The suppression of convective heat transfer by the magnetic field limits the thermal energy delivered to NEPCM particles, thereby reducing the spatial extent of the phase change region and decreasing the system's ability to utilize latent heat storage effectively.

Fig. 10 demonstrates how Reynolds and Richardson numbers impact on transferring the mass and heat characteristics, represented by mean Nusselt (Nu_{av}) number and Sherwood (Sh_{av}) number. At low Reynolds number, the impact of Richardson number is minimal, showing only a 1.39 % increase in Nu_{av} (from 4.6174 to 4.6815) as Ri increases from 0.1 to 7. However, at higher Reynolds numbers, the influence of Ri becomes more pronounced. At $Re = 100$, Nu_{av} increases significantly by 192.77 % (from 4.8775 to 14.27) over the same Ri range. Similarly, the Sherwood number exhibits comparable behavior, with a minimal increase of 0.42 % at $Re = 10$ and a substantial rise of 141.23 % at $Re = 100$ when Ri varies from 0.1 to 7. This behavior can be explained through the interaction of natural and forced convective flow. At low Reynolds numbers, forced convection is weak, and the buoyancy effect (represented by Ri) has limited influence on the flow field. As Reynolds number increases, the stronger forced convection interacts more effectively with buoyancy forces, enhancing mass and heat transfer rates. In light of the larger gain in Nu_{av} versus Sh_{av} (192.77 % versus 141.23 % at $Re = 100$) indicates that thermal transport is more sensitive to these combined effects than mass transfer, likely due to the additional influence of NEPCM thermal properties and magnetic field presence (Ha = 10), since it primarily affects the momentum and energy transport mechanisms.

Fig. 11 illustrates the effect of Richardson number (Ri) and Reynolds number (Re) on Bejan number (Be) and the total entropy produced (S_{total}). The entropy production shows an increasing trend with both Re and Ri, with the most dramatic changes occurring at higher values of both parameters. At $Re = 10$, the total entropy increases marginally by 1.39 % (from 4.7321 to 4.7979) as Ri increases from 0.1 to 7. However, at $Re = 100$, a substantial increase of 191.13 % (from 4.9981 to 14.551) is observed over the same Ri range. Conversely, the Bejan number tends to decrease with increased Re and Ri, emphasizing that thermal irreversibility is more important than fluid friction irreversibility. At $Re =$ 10, Be decreases slightly by 0.11 % (from 0.98844 to 0.98738), while at $Re = 100$, a more significant reduction of 5.81 % (from 0.97178 to 0.91532) is observed as Ri increases from 0.1 to 7. This behavior is a result of intensification in fluid mixing along with temperature gradients at greater Re and Ri values. The substantial increase in total entropy generation reflects enhanced irreversibility due to stronger convective effects and greater fluid friction. The decreasing Bejan number indicates that fluid friction irreversibility becomes increasingly dominant compared to thermal irreversibility as both forced convection (Re) and buoyancy effects (Ri) strengthen. This transition is particularly pronounced at higher Reynolds numbers where the enhanced fluid mixing leads to more significant viscous dissipation effects.

Fig. 12 displays how buoyancy ratio and Lewis number relate to heat and mass transfer. Increasing Le results a non-monotonic behavior in mean Nusselt number; It reaching peak values at Le = 1 across all buoyancy ratios. For instance, at Nz = 2, Nu_{av} increases by 6.36 % as Le rises from 0.1 to 1 (from 5.2997 to 5.6368), followed by a decrease of 8.12 % as Le further increases to 10 (dropping to 5.1793). In contrast, the Sherwood number exhibits a consistent increasing trend with Le, showing a substantial rise of 94.81 % (from 3.7293 to 8.055) at Nz = 2 as Le increases from 0.1 to ten. The influence of buoyancy factor is consistently positive for both parameters, though with varying intensities. At Le = 1, a Nz increase from one to five yields a 29.06 % gain in Nu_{av} (from 5.21 to 6.7241) and a 30.84 % increase in Sh_{av} (from 4.2363 to 5.5428). Solutal buoyancy and heat forces are thought to interact complexly to cause a behaviour like this. The peak in Nu_{av} at Le

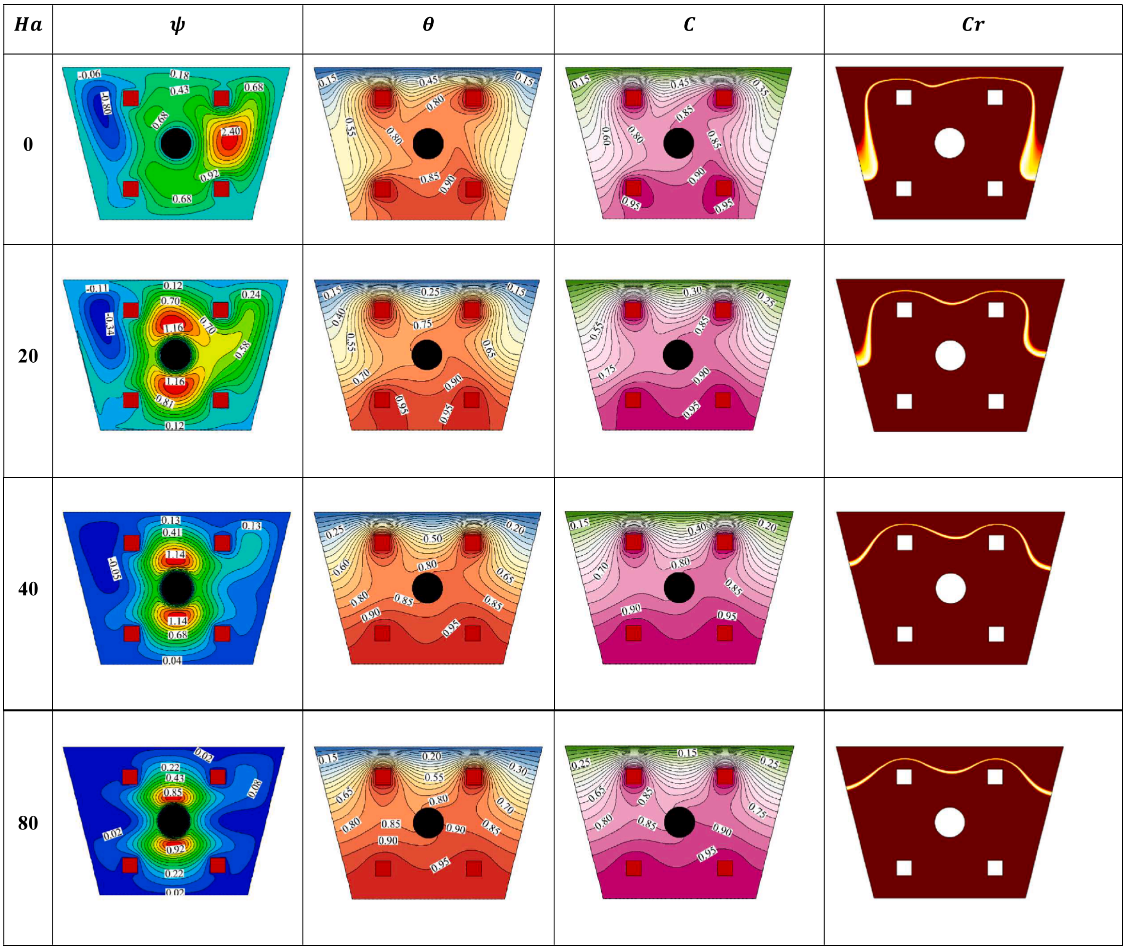

Fig. 9. Contours of ψ, θ, C *and* Cr for different Ha at $Ri = 1$, $Re = 50$, $Le = 0.5$, $\phi = 0.01$, $Nz = 2$, and $Ste = 0.1$.

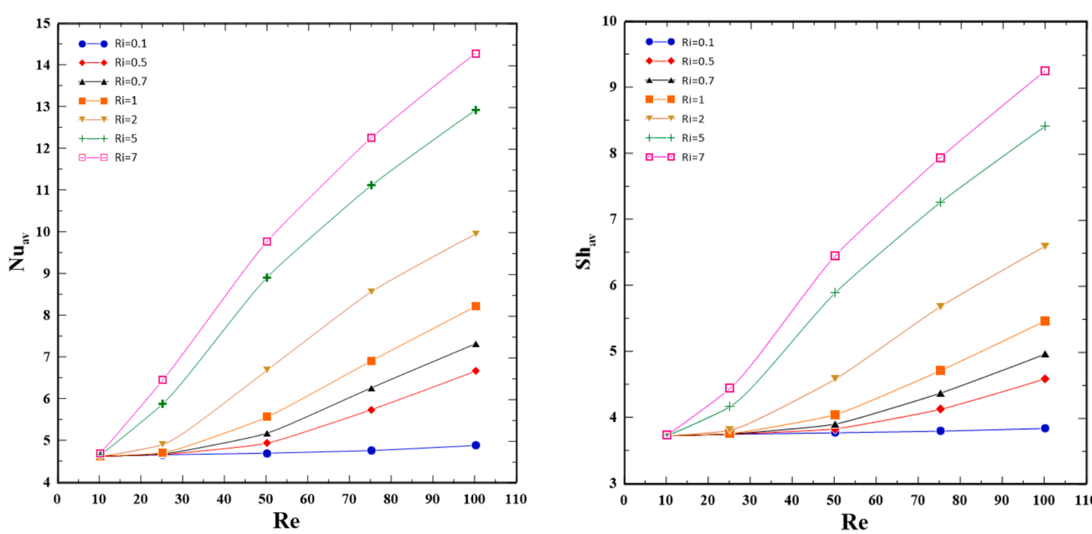

Fig. 10. Impact of Ri and Re on Nu_{av} and Sh_{av} at $Nz = 2$, $Le = 0.5$, $Ste = 0.1$, $\phi = 0.01$, $\Theta_f = 0.5$, *and* $Ha = 10$.

= 1 represents an optimal balance between mass diffusion and thermal rates, while Sh_{av} continuously increases with Le, reflects the enhanced species diffusion capability of the fluid. The stronger effect of Nz at moderate Lewis numbers suggests an optimal coupling between double-diffusive convection mechanisms under these conditions.

Fig. 13 reveals the combined influence of buoyancy ratio and Lewis number on entropy generation characteristics. The total entropy generation (S_{total}) exhibits behavior similar to the heat transfer patterns, showing a peak at Le = 1 before declining at higher Lewis numbers. For Nz = 2, S_{total} increases by 6.39 % as Le rises from 0.1 to 1 (from 5.4333 to 5.78), followed by a decrease of 8.21 % as Le further increases to 10 (reducing to 5.3057). This trend is consistent across all buoyancy ratios,

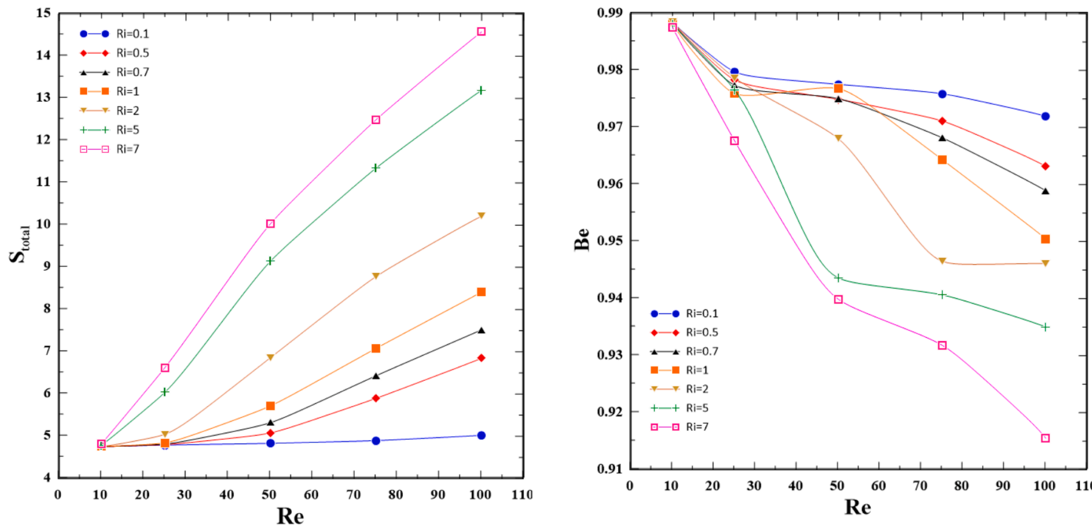

Fig. 11. Impact of Re and Ri on S_{total} & Be at $Nz = 2,\ Le = 0.5,\ Ste = 0.1,\ \phi = 0.01,\ \Theta_f = 0.5,\ and\ Ha = 10.$

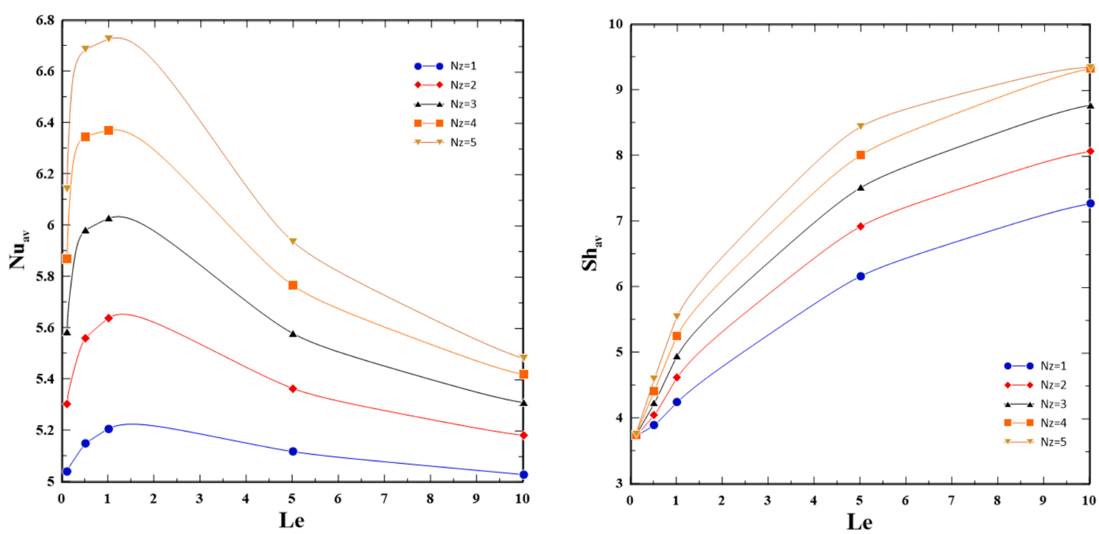

Fig. 12. Impact of Nz, and Le on Nu_{av} & Sh_{av} at $Ri = 1,\ Re = 50,\ Ste = 0.1,\ \phi = 0.01,\ \Theta_f = 0.5,\ and\ Ha = 10.$

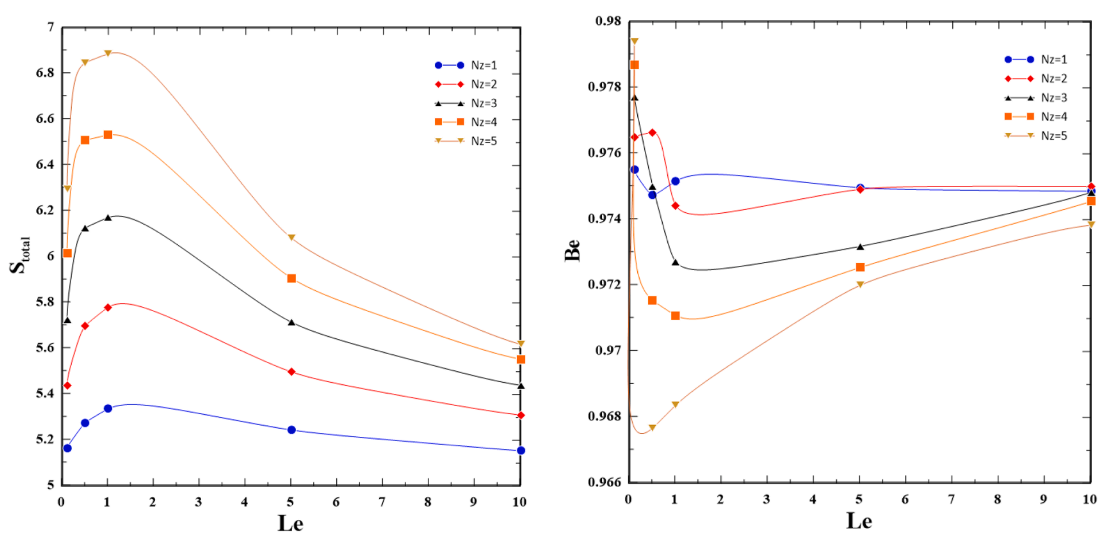

Fig. 13. Impact of Nz and Le on S_{total}, Be at $Ri = 1,\ Re = 50,\ Ste = 0.1,\ \phi = 0.01,\ \Theta_f = 0.5,\ and\ Ha = 10.$

though with varying intensities. The Bejan number shows subtle but noteworthy variations with both parameters. At moderate Lewis numbers (Le = 0.5), Be experiences a maximum of 0.97662 at Nz = 2, followed by a gradual decline to 0.968 at Nz = 5, representing a decrease of 0.89 %. As a result of these conditions, thermal irreversibility contributes to the production of total entropy at its maximum. At higher Lewis numbers (Le = 10), the Bejan number shows more stability across different buoyancy ratios, varying only by 0.11 % (from 0.97483 to 0.9738) as Nz increases from 1 to 5. These patterns can be explained by the competing effects of thermal and solutal transport mechanisms. The peak in total entropy generation at Le = 1 corresponds to conditions where thermal and mass diffusion rates are balanced, leading to maximum irreversibility. The relatively stable Bejan number at higher Lewis numbers suggests that the proportion of thermal to viscous irreversibilities remains fairly constant, despite changes in the buoyancy ratio, indicating a well-established balance between different transport mechanisms.

Fig. 14 illustrates the effects of Stefan number (Ste), and fusion temperature (θ_f) in terms of heat transfer and mass transfer characteristics. The average Nusselt number shows maximum values at intermediate fusion temperatures ($\theta_f = 0.5$) for all Stefan numbers, with the effect being most pronounced at Ste = 0.1, where Nu_av increases by 3.11 % from $\theta_f = 0.1$ to 0.5 (from 5.39 to 5.5578) before decreasing by 2.41 % as θ_f increases to 0.9 (to 5.424). The influence of Stefan number is consistently negative, with Nu_{av} showing a decrease of 2.80 % (from 5.5578 to 5.4023) at $\theta_f = 0.5$ as Ste increases from 0.1 to 0.8. The Sherwood number exhibits remarkably stable behavior across all parametric variations, with changes <0.1 % for both θ_f and Ste variations. This stability suggests that mass transfer characteristics are relatively insensitive to phase change parameters under the given conditions. This behavior can be attributed to the dominating role played by Lewis number as well as buoyancy factor in mass transfer processes. The observed trends can be explained by NEPCM particles' change phase dynamics. At intermediate fusion temperatures, the latent and sensible heat transfer mechanisms are balanced. The decreasing trend with increasing Stefan number indicates that higher latent heat capacity (lower Ste) improves thermal transfer effectiveness, possibly through improved thermal storing and release during phase changes.

Fig. 15 explains how Stefan number and fusion temperature affect entropy generation characteristics. The total entropy generation (S_{total}) exhibits behavior similar to heat transfer patterns, showing peak values at intermediate fusion temperatures. S_total increases at Ste = 0.1, by 3.19 % from $\theta_f = 0.1$ to 0.5 (from 5.5237 to 5.70), followed by a decrease of 2.46 % as θ_f increases to 0.9 (to 5.56). The Stefan number shows a consistent negative impact on entropy generation, with S_{total} decreasing by 2.88 % (from 5.70 to 5.536) at $\theta_f = 0.5$ as Ste increases from 0.1 to 0.8. The Bejan number remains remarkably stable across all parameter variations, showing variations of <0.1 %. This stability indicates that the relative contributions of thermal and viscous irreversibilities remain nearly constant regardless of phase change conditions. At $\theta_f = 0.5$, Be varies minimally from 0.977 to 0.97656 as Ste alters (range between 0.1 and 0.8), suggesting a stable balance between different irreversibility mechanisms. A phase change's thermodynamic nature can explain this behavior. At intermediate fusion temperatures, the maximum generation of entropy occurs at conditions where phase change effects are most active, resulting in enhanced irreversibility through simultaneous transfer of sensible and latent heat. The decreasing trend with increasing Stefan number indicates that higher latent heat capacity contributes to reduced system irreversibility, likely due to more efficient thermal energy storage and release mechanisms.

Fig. 16 shows how NEPCM volume fraction along with Hartmann number influence mass and thermal transfer. The average Nusselt number shows a consistently increasing trend with volume fraction across all Hartmann numbers. At Ha = 10, Nu_{av} increases by 33.77 % (from 6.0674 to 8.1163) as ϕ increases from 0.015 to 0.035. However, Hartmann number increases suppress thermal transfer, with Nu_{av} decreasing by 16.44 % (from 6.0674 to 5.07) at ϕ = 0.015 as Ha increases from 10 to 80. In contrast, the Sherwood number exhibits minimal sensitivity to changes in NEPCM volume fraction, showing variations of <0.1 % across the entire range of ϕ. However, it demonstrates significant dependence on the Hartmann number, decreasing by 7.82 % (from 4.04 to 3.7239) at ϕ = 0.02 as Ha increases from 10 to 80. This behavior can be explained by the competing mechanisms of magnetic damping and enhanced thermal conductivity. As the NEPCM concentration increases, Nu_{av} increases due to the improved mixture thermal conduction. In contrast, higher magnetic fields (higher Ha) suppress fluid movement through electromagnetic damping, which reduces mass transfer and thermal transfer. Species transport appears more dependent on flow field characteristics than thermal properties, owing to a relatively insensitive relationship between transfer of mass and NEPCM concentration.

Fig. 17 demonstrates the effects of NEPCM volume fraction (ϕ) and Hartmann number (Ha) on entropy generation characteristics. Total entropy generation (S_{total}) shows a decreasing trend with both parameters. As ϕ increases from 0.015 to 0.035 at Ha = 10, S_{total} decreases by 1.42 % (from 5.6664 to 5.5862). A more pronounced reduction of 16.41 % (from 5.6664 to 4.7359) is observed when Ha rises from 10 to 80 at ϕ

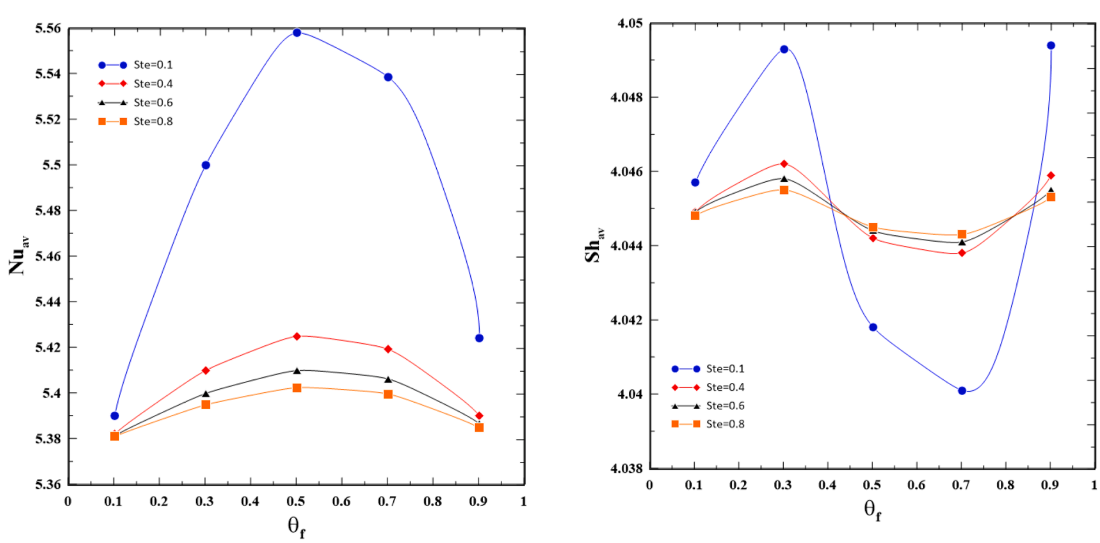

Fig. 14. Impact of Θ_f and Ste on Nu_{av} and Sh_{av} for $Ri = 1,\ Re = 50,\ Le = 0.5,\ \phi = 0.01,\ Nz = 2,\ and\ Ha = 10.$

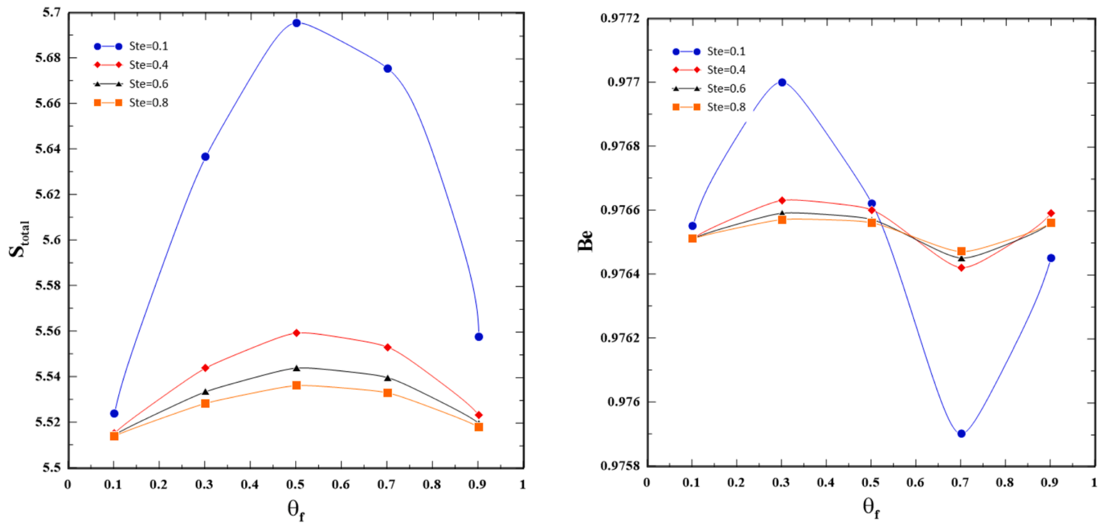

Fig. 15. Impact of Θ_f and *Ste* on S_{total} and *Be* for $Ri = 1,\ Re = 50,\ Le = 0.5,\ \phi = 0.01,\ Nz = 2,\ and\ Ha = 10.$

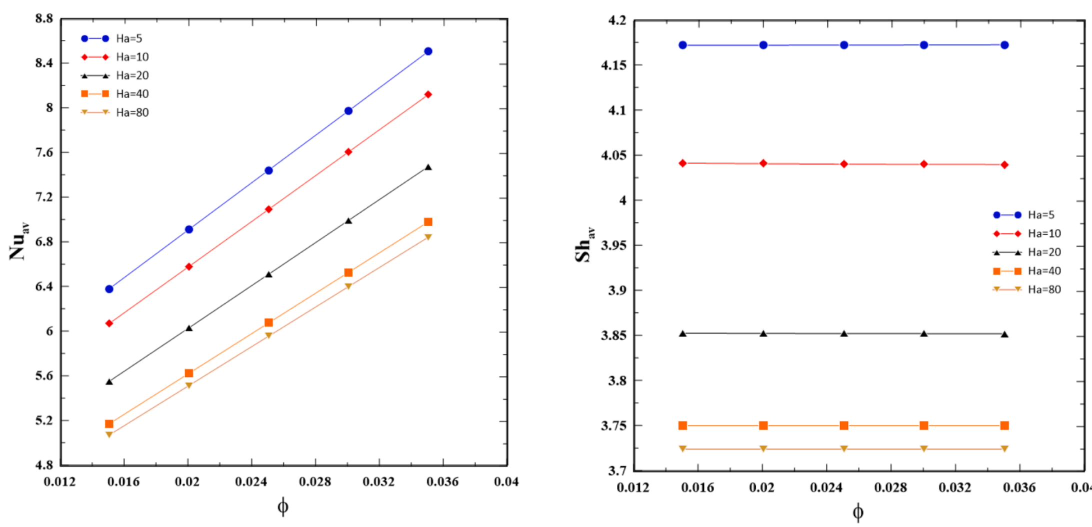

Fig. 16. Impact of ϕ and *Ha* on Nu_{av} and Sh_{av} for $Re = 50,\ Ri = 1,\ Le = 0.5,\ Nz = 2, \Theta_f = 0.5,\ and\ Ste = 0.1.$

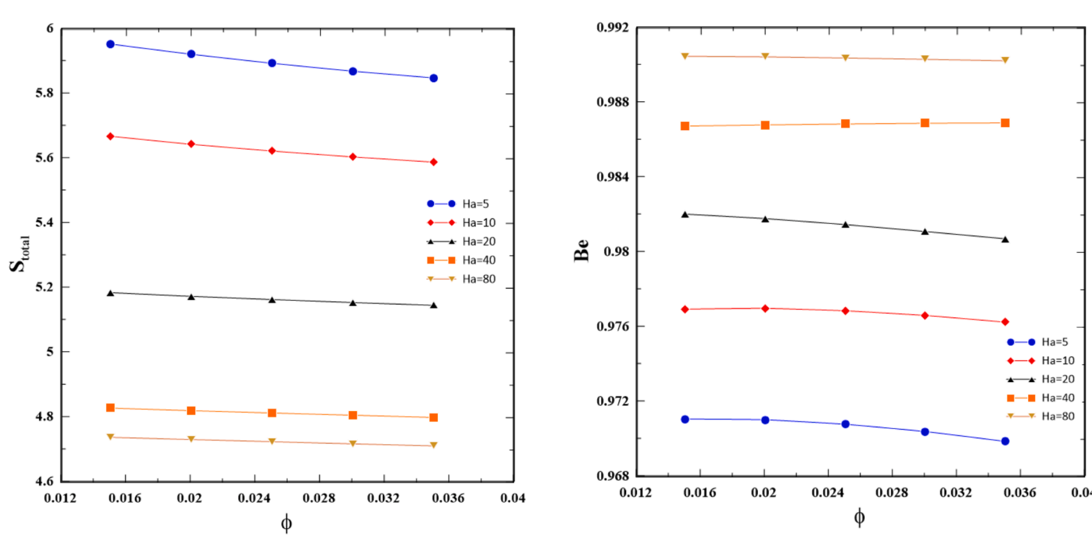

Fig. 17. Impact of ϕ and *Ha* on S_{total} and *Be* for $Re = 50,\ Ri = 1,\ Le = 0.5,\ Nz = 2, \Theta_f = 0.5,\ and\ Ste = 0.1.$

= 0.015. It is interesting to note the inverse relationship between Bejan number and these parameters. While increasing ϕ causes a slight decrease in Be (0.07 % reduction from 0.9769 to 0.97621 at Ha = 10), increasing Ha leads to a notable rise in Be (1.38 % increase from 0.9769 to 0.99043 at ϕ = 0.015). This behavior indicates a shift in the dominant irreversibility mechanism with changing magnetic field strength. These trends can be attributed in part to a suppression of fluid motion by the magnetic field and a NEPCM's influence on transport properties. The decrease in total entropy generation with increasing Ha reflects reduced fluid mixing and associated irreversibilities due to magnetic damping. The rising Bejan number with Ha suggests that thermal irreversibility becomes increasingly dominant compared to fluid friction irreversibility under stronger magnetic fields, likely due to the suppression of velocity gradients while maintaining temperature gradients.

The present findings provide several insights that advance understanding beyond existing literature on NEPCM-based cooling systems. While previous studies have independently examined either MHD effects or NEPCM applications in thermal management, this investigation quantifies their coupled influence in electronic cooling configurations. The 192.77 % enhancement in heat transfer through optimal *Re*-Ri combinations demonstrates that buoyancy-assisted mixed convection can substantially improve cooling effectiveness, consistent with recent findings by Hassan et al. [66] and Alomari et al. [67]on double-diffusive systems. However, the present study extends these findings by demonstrating that magnetic field strength provides a controllable mechanism for optimizing the balance between heat transfer enhancement and entropy minimization. The observed 16.41 % reduction in total entropy generation with increasing Hartmann number, while maintaining acceptable heat transfer rates, suggests that moderate magnetic damping can improve thermodynamic efficiency by suppressing viscous irreversibilities more than it reduces thermal transport. This finding contrasts with earlier works that focused primarily on heat transfer maximization without considering entropy optimization. Furthermore, the identification of optimal fusion temperature (θ_f = 0.5) and the demonstration that NEPCM concentration enhances heat transfer by 33.77 % while simultaneously reducing entropy generation provides practical design guidelines not previously established in the literature. The non-monotonic behavior of heat transfer with Lewis number, peaking at Le = 1, reveals an optimal balance between thermal and mass diffusion mechanisms that has not been systematically characterized in combined NEPCM-MHD systems. These results collectively demonstrate that effective electronic thermal management requires careful parametric optimization considering the competing effects of electromagnetic damping, phase change dynamics, and double-diffusive transport, providing a framework for designing energy-efficient cooling systems that maximize heat dissipation while minimizing thermodynamic irreversibilities.

5. Conclusions

The purpose of this study was to investigate entropy generation and hydrothermal performance of a trapezoidal chamber containing NEPCM-water mixture in the presence of a magnetic field and double-diffusive mixed convection. This study will conclude with the following findings:

1. Combined effects of Reynolds and Richardson numbers demonstrate considerable enhancement of thermal transfer, with Nu_{av} increasing by 192.77 % (from 4.8775 to 14.27) at *Re* = 100 when Ri varies from 0.1 to 7, indicating that natural and forced convection are tightly coupled.
2. While Lewis number does not show a monotonic relationship with heat transfer, it consistently shows a positive impact on transferring mass, with Sh_{av} increasing by 94.81 % (from 3.7293 to 8.055) at Nz = 2 as Le increases from 0.1 to 10.
3. Phase change parameters show optimal performance at intermediate fusion temperatures (θ_f = 0.5), with Nu_{av} increasing by 3.11 % compared to θ_f = 0.1, while the Stefan number demonstrates a negative impact on heat transfer performance.
4. NEPCM concentration significantly enhances heat transfer (33.77 % increase in Nu_{av} for ϕ = 0.015 to 0.035 at Ha = 10), while magnetic field strength shows a suppressive effect (16.44 % decrease in Nu_{av} as Ha reaches 80).
5. Under the same conditions, the total production of entropy decreases with both NEPCM concentration and magnetic field strength, with a notable 16.41 % reduction when Ha increases to 80, whereas the Bejan number increases by 1.38 %.

This investigation sheds light on how to optimize electronic cooling devices utilizing NEPCM under magnetic field influence. The findings offer practical guidelines for designing more efficient cooling systems by identifying optimal operating parameters and understanding the trade-offs between thermal transfer enhancement and the generation of entropy. The results are particularly pertinent to applications in electronic thermal management where both cooling effectiveness and system efficiency are crucial considerations. Developing energy conserving and increasing sustainability of cooling solutions for electronic devices requires a comprehensive examination of entropy generation characteristics and double diffusion transport.

CRediT authorship contribution statement

Ahmed M. Hassan: Writing – original draft, Validation, Supervision. **Mohammed Azeez Alomari:** Writing – original draft, Software, Project administration, Methodology, Investigation. **Mohammad Ghalambaz:** Writing – review & editing, Project administration, Methodology. **Omaima Jabbar:** Visualization, Validation, Software. **Faris Alqurashi:** Validation, Resources, Project administration, Investigation. **Mujtaba A. Flayyih:** Software, Investigation, Funding acquisition, Formal analysis.

Declaration of competing interest

This paper's authors declare they do not have any competing financial interests or personal relationships that could have influenced their findings.

Acknowledgements

A special thanks goes out to Qatar National Library for its support of open access.

It is the authors' sincere gratitude to the University of Bisha's Deanship of Scientific Research for funding this research.

Data availability

Data will be made available on request.

References

[1] M. Kim, T. Kim, H. You, C. Kim, Y.-S. Han, B.-I. Choi, K.H. Do, Mixed convection model for predicting the Nusselt number of oscillating vertical plates, Int. J. Heat. Mass Transf. 234 (2024) 126118, https://doi.org/10.1016/j.ijheatmasstransfer.2024.126118.

[2] K. Motegi, Y. Sibamoto, T. Hibiki, Reynolds-averaged Navier-Stokes simulations of opposing flow turbulent mixed convection heat transfer in a vertical tube, Int. J. Heat. Mass Transf. 237 (2025) 126406, https://doi.org/10.1016/j.ijheatmasstransfer.2024.126406.

[3] A. Tanveer, H. Sami ul, M.B. Ashraf, J. Ro, Thermal analysis of nonlinear mixed convection effects within wavy enclosure, Case Stud. Therm. Eng. 63 (2024) 105322, https://doi.org/10.1016/j.csite.2024.105322.

[4] Hai, T., I. Omar, A. a. Alizadeh, N. Varshney, S. Dixit, A.J. Sultan, A.E. Anqi, S. Bhatnagar, H. Rajab, and N.J.S.R. Singh Sawaran Singh, Optimization of nano-

finned enclosure-shaped latent heat thermal energy storage units using CFD, RSM, and enhanced hill climbing algorithm. 15 (1) (2025) 12486.

[5] A.M. Hassan, M.A. Alomari, Q.H. Al-Salami, F.A. Alyousuf, F. Alqurashi, M. A. Flayyih, Numerical analysis of hydrothermal performance and entropy generation in an active cooling system: a case study with NEPCM, double-diffusive mixed-convection and MHD, Case Stud. Therm. Eng. 61 (2024) 105064, https://doi.org/10.1016/j.csite.2024.105064.

[6] W. Tian, T. Peng, X. Fan, Y. Tang, D. Fan, Y. Wang, X. Liu, H. Meng, L. Gu, Numerical analysis of turbulent mixed convection heat transfer of molten salt in horizontal tubes with uniformly cooled heat flux, Int. J. Heat. Mass Transf. 228 (2024) 125630, https://doi.org/10.1016/j.ijheatmasstransfer.2024.125630.

[7] Z. Ullah, E.R. El-Zahar, L.F. Seddek, N. Becheikh, B.M. Alshammari, M. S. Aldhabani, L. Kolsi, Solar radiation and heat sink impact on fluctuating mixed convective flow and heat rate of darcian nanofluid: applications in electronic cooling systems, Case Stud. Therm. Eng. 59 (2024) 104592, https://doi.org/10.1016/j.csite.2024.104592.

[8] Y.-M. Chu, U. Farooq, N.K. Mishra, Z. Ahmad, F. Zulfiqar, S. Yasmin, S.A. Khan, CFD analysis of hybrid nanofluid-based microchannel heat sink for electronic chips cooling: applications in nano-energy thermal devices, Case Stud. Therm. Eng. 44 (2023) 102818, https://doi.org/10.1016/j.csite.2023.102818.

[9] A. Aissa, A. Belazreg, H. Laidoudi, S. Mohammed, O. Younis, A.J.C.S.i.T. E. Alazzam, Enhanced heat transmission in a triangular enclosure with a rotating cooled wall using Nano-encapsulated Phase Change Material nanofluid under mixed convection, Case Stud. Therm. Eng. 54 (2024) 103992, https://doi.org/10.1016/j.csite.2024.103992.

[10] D.-H. Shin, C.S. Kim, G.-C. Park, H.K. Cho, Experimental analysis on mixed convection in reactor cavity cooling system of HTGR for hydrogen production, Int J Hydrog. Energy 42 (34) (2017) 22046–22053, https://doi.org/10.1016/j.ijhydene.2017.06.232.

[11] L. Liu, D. Zhang, L. Li, Y. Yang, C. Wang, S. Qiu, G.H. Su, Experimental investigation of flow and convective heat transfer on a high-Prandtl-number fluid through the nuclear reactor pebble bed core, Appl. Therm. Eng. 145 (2018) 48–57, https://doi.org/10.1016/j.applthermaleng.2018.09.017.

[12] A. Abdelmaksoud, H.F. Elbakhshawangy, O.S. Abd El-Kawi, Heat transport and chimney design in a typical MTR reactor during natural convection cooling regime, Prog. Nucl. Energy 138 (2021) 103814, https://doi.org/10.1016/j.pnucene.2021.103814.

[13] C. Dong, G. Lu, R. Chen, K. Zhang, C. Liu, W. Tian, S. Qiu, G.H. Su, Heat transfer of air turbulent mixed convection in the passive containment air-cooling system of a modular small nuclear reactor, Int. J. Therm. Sci. 182 (2022) 107793, https://doi.org/10.1016/j.ijthermalsci.2022.107793.

[14] Kassim, M.S., A. Oleiwi, D.S. Khudhur, L.J.J.J.o.M.E.R. Habeeb, and Developments, Three dimensional study of baffles effect on heat transfer in shell and tube heat exchanger. 43 (5) (2020) 332–345.

[15] J.P. Ekka, P. Muthukumar, Exergy efficiency and sustainability indicators of forced convection mixed mode solar dryer system for drying process, Renew. Energy 234 (2024) 121256, https://doi.org/10.1016/j.renene.2024.121256.

[16] Ali, A.A., D. Alfarge, F. lafta Rashid, A.A. Ugla, A. Kareem, and H.I.J.G. Mohammed, Improving photovoltaic panels by utilizing ground-coupled heat exchangers: insights and technological advances. 130 (2025) 103335.

[17] Rasheed, R.H., A.S. Sadeq, M.N. Fares, S. Salahshour, R.J.C.S.i.C. Sabetvand, and E. Engineering, Modeling the thermal performance of hybrid paraffin-air nanostructure in a heat sink: effect of atomic ratio of Al 2 O 3 nanoparticles. 11 (2025) 101109.

[18] Ali, A.B., S.F. Alhamdi, M.M. Al-Azawii, N.S.S. Singh, M.A. Fazilati, S. Salahshour, and S.A.J.R.i.E. Eftekhari, Thermal management in a phase change material-based microchannel heat sink manifold system for cooling electronic boards. 26 (2025) 104914.

[19] Said, M.A., H.S.S. Aljibori, A.M. Abed, H. Togun, H.I. Mohammed, J.M. Mahdi, A. Rahbari, A.M. Sadeq, and P.J.C.S.i.T.E. Talebizadehsardari, Innovative pipe profile configurations for fast charging of phase change material in compact thermal storage systems for building heating applications. 69 (2025) 106036.

[20] A.A. Alwan, A.M.J.A.J.f.S. Hassan, Engineering, Experimental study on optimizing photovoltaic panel efficiency: harnessing paraffin wax phase change for temperature reduction, Arab. J. Sci. Eng. (2024) 1–14, https://doi.org/10.1007/s13369-023-08581-3.

[21] X. Li, G. Fan, Entropy analysis and MHD mixed convection heat transfer of the magnetic nanofluid in an asymmetric T-shaped cavity using the lattice Boltzmann method, Eng. Anal. Bound. Elem. 157 (2023) 229–238, https://doi.org/10.1016/j.enganabound.2023.09.012.

[22] R.H. Hameed, B.M. Al-Srayyih, Q.R. Al-Amir, H.K. Hamzah, F.H. Ali, A. Alahmer, Magnetic field effect on mixed convection flow inside an oval-shaped annulus enclosure filled by a non-Newtonian nanofluid, Int. J. Thermofluids 21 (2024) 100571, https://doi.org/10.1016/j.ijft.2024.100571.

[23] S.E. Ahmed, Z.A.S. Raizah, A. Chamkha, Mixed convective transport in inclined porous open arc-shaped enclosures saturated by nanofluids using a second-order Boussinesq approximation, Case Stud. Therm. Eng. 27 (2021) 101295, https://doi.org/10.1016/j.csite.2021.101295.

[24] A.I. Alsabery, M. Vaezi, T. Tayebi, I. Hashim, M. Ghalambaz, A.J. Chamkha, Nanofluid mixed convection inside wavy cavity with heat source: a non-homogeneous study, Case Stud. Therm. Eng. 34 (2022) 102049, https://doi.org/10.1016/j.csite.2022.102049.

[25] A.I. Alsabery, M.A. Sheremet, A.J. Chamkha, I. Hashim, Impact of nonhomogeneous nanofluid model on transient mixed convection in a double lid-driven wavy cavity involving solid circular cylinder, Int. J. Mech. Sci. 150 (2019) 637–655, https://doi.org/10.1016/j.ijmecsci.2018.10.069.

[26] F.M. Azizul, A.I. Alsabery, I. Hashim, Heatlines visualisation of mixed convection flow in a wavy heated cavity filled with nanofluids and having an inner solid block, Int. J. Mech. Sci. 175 (2020) 105529, https://doi.org/10.1016/j.ijmecsci.2020.105529.

[27] Z. Li, P. Barnoon, D. Toghraie, R.B. Dehkordi, M. Afrand, Mixed convection of non-newtonian nanofluid in an H-shaped cavity with cooler and heater cylinders filled by a porous material: two phase approach, Adv. Powder Technol. 30 (11) (2019) 2666–2685.

[28] N. Rehman, R. Mahmood, A.H. Majeed, M.R. Ali, A.S. Hendy, Enhanced heat transfer in vented square enclosures with block structures: exploring iso-perimetric shapes and multigrid approach for mixed convection of nano-fluids, Case Stud. Therm. Eng. 58 (2024) 104391, https://doi.org/10.1016/j.csite.2024.104391.

[29] R. Jain, R. Mehta, A. Bhatnagar, H. Ahmad, Z.A. Khan, G.M. Ismail, Numerical study of heat and mass transfer of williamson hybrid nanofluid (CuO/CNT's-water) past a permeable stretching/shrinking surface with mixed convective boundary condition, Case Stud. Therm. Eng. 59 (2024) 104313, https://doi.org/10.1016/j.csite.2024.104313.

[30] H. Ali Madkhali, M. Haneef, A.S. El-Shafay, S.O. Alharbi, M. Nawaz, Mixed convective transport in Maxwell hybrid nano-fluid under generalized Fourier and Fick laws, Int. Commun. Heat Mass Transf. 130 (2022) 105714, https://doi.org/10.1016/j.icheatmasstransfer.2021.105714.

[31] F.A. Abood, Z.K. Radhi, A.K. Hadi, R.Z. Homod, H.I. Mohammed, MHD mixed convection of nanofluid flow Ag- Mgo/water in a channel contain a rotational cylinder, Int. J. Thermofluids 22 (2024) 100713, https://doi.org/10.1016/j.ijft.2024.100713.

[32] M.A. Alomari, A.M. Hassan, A. Alajmi, A.M. Sadeq, F. Alqurashi, M.A.J.I.C.i. H. Flayyih, M. Transfer, A comprehensive numerical analysis of heat transfer enhancement in NEPCM-water mixtures using oscillating fin and oriented magnetic fields, Int. Commun. Heat Mass Transf. 161 (2025) 108455, https://doi.org/10.1016/j.icheatmasstransfer.2024.108455.

[33] F. Yuan, W. Yu, J. Lin, Numerical study of the effects of nanorod aspect ratio on poiseuille flow and convective heat transfer in a circular minichannel, Microfluid. Nanofluidics. 24 (8) (2020) 62, https://doi.org/10.1007/s10404-020-02370-2.

[34] A. Zaraki, M. Ghalambaz, A.J. Chamkha, M. Ghalambaz, D. De Rossi, Theoretical analysis of natural convection boundary layer heat and mass transfer of nanofluids: effects of size, shape and type of nanoparticles, type of base fluid and working temperature, Adv. Powder Technol. 26 (3) (2015) 935–946, https://doi.org/10.1016/j.apt.2015.03.012.

[35] P. Sudarsana Reddy, A.J. Chamkha, Influence of size, shape, type of nanoparticles, type and temperature of the base fluid on natural convection MHD of nanofluids, Alex. Eng. J. 55 (1) (2016) 331–341, https://doi.org/10.1016/j.aej.2016.01.027.

[36] H. Behzadnia, H. Jin, M. Najafian, M. Hatami, Investigation of super-critical water-based nanofluid with different nanoparticles (shapes and types) used in the rectangular corrugated tube of reactors, Alex. Eng. J. 61 (3) (2022) 2330–2347, https://doi.org/10.1016/j.aej.2021.06.083.

[37] F. Selimefendigil, H.F. Öztop, N. Abu-Hamdeh, Mixed convection due to rotating cylinder in an internally heated and flexible walled cavity filled with SiO2–water nanofluids: effect of nanoparticle shape, Int. Commun. Heat Mass Transf. 71 (2016) 9–19, https://doi.org/10.1016/j.icheatmasstransfer.2015.12.007.

[38] H. Zhang, X. Nie, D.O. Bokov, D. Toghraie, O.A. Akbari, F. Montazerifar, F. Pourfattah, Y. Esmaeili, R. Khodaparast, Numerical study of mixed convection and entropy generation of water-Ag nanofluid filled semi-elliptic lid-driven cavity, Alex. Eng. J. 61 (11) (2022) 8875–8896, https://doi.org/10.1016/j.aej.2022.02.028.

[39] M. Rajarathinam, N. Nithyadevi, A.J. Chamkha, Heat transfer enhancement of mixed convection in an inclined porous cavity using Cu-water nanofluid, Adv. Powder Technol. 29 (3) (2018) 590–605, https://doi.org/10.1016/j.apt.2017.11.032.

[40] H. Li, Y. Zhuang, J.-C. Feng, S.-M. Huang, Experimental study on the solidification and melting performances of magnetic NEPCMs composited with optimized filling metal foam in a uniform magnetic field, Sol. Energy 263 (2023) 111927, https://doi.org/10.1016/j.solener.2023.111927.

[41] R. Hidki, L. El Moutaouakil, M. Boukendil, Z. Charqui, Z. Zrikem, A. Abdelbaki, Natural convection heat transfer analysis of a nano-encapsulated phase change material (NEPCM) confined in a porous square chamber with two heat sources, J. Energy Storage 73 (2023) 108924, https://doi.org/10.1016/j.est.2023.108924.

[42] M.A. Alomari, A.M. Hassan, Q.H. Al-Salami, F.Q. Alyousuf, F. Alqurashi, M.A.J.I.C. i.H. Flayyih, M. Transfer, Convection flow of NE-phase change material-water mixture in evacuated tube solar collector manifold: numerical analysis of MHD double-diffusive convection and exothermic reaction, Int. Commun. Heat Mass Transf. 159 (2024) 108194, https://doi.org/10.1016/j.icheatmasstransfer.2024.108194.

[43] A.M. Hassan, M.A. Alomari, A. Alajmi, A.M. Sadeq, F. Alqurashi, M.A.J.R.i. E. Flayyih, Numerical analysis of nano-encapsulated PCM magnetohydrodynamics double-diffusive convection and entropy generation in vertical enclosures with porous layer, Results Eng. (2024) 103579, https://doi.org/10.1016/j.rineng.2024.103579.

[44] K. Irshad, A.A. Pasha, M.K. Al Mesfer, M. Danish, M.K. Nayak, A.J. Chamkha, A. M. Galal, Hydrothermal behavior and entropy analysis of double-diffusive nano-encapsulated phase change materials in a porous wavy H-shaped cavity with baffles: effect of thermal parameters, J. Energy Storage 72 (2023) 108250, https://doi.org/10.1016/j.est.2023.108250.

[45] Herouz, K., H. Laidoudi, A. Aissa, A. Mourad, K. Guedri, M. Oreijah, and O.J.J.o.E. S. Younis, Analysis of nano-encapsulated phase change material confined in a double lid-driven hexagonal porous chamber with an obstacle under magnetic field. 61 (2023) 106736.

[46] Z. Raizah, A.M.J.C.S.i.T.E. Aly, Double-diffusive convection of a rotating circular cylinder in a porous cavity suspended by nano-encapsulated phase change materials, Case Stud. Therm. Eng. 24 (2021) 100864.
[47] C.J. Ho, Y.-C. Liu, M. Ghalambaz, W.-M. Yan, Forced convection heat transfer of Nano-encapsulated phase change material (NEPCM) suspension in a mini-channel heatsink, Int. J. Heat. Mass Transf. 155 (2020) 119858, https://doi.org/10.1016/j.ijheatmasstransfer.2020.119858.
[48] R. Hidki, L. El Moutaouakil, M. Boukendil, Z. Charqui, B. Jamal, Application of an artificial intelligence model for natural convection of nano-encapsulated phase change materials (NEPCMs) confined in a porous square enclosure with an inclined elliptical heated block, Int. Commun. Heat Mass Transf. 155 (2024) 107546, https://doi.org/10.1016/j.icheatmasstransfer.2024.107546.
[49] A. Abderrahmane, H. Laidoudi, A. Belazreg, O. Younis, Magneto-convection flow of nano-encapsulated phase change material (NEPCM) confined within a trapezoidal porous enclosure, Int. J. Thermofluids 24 (2024) 100828, https://doi.org/10.1016/j.ijft.2024.100828.
[50] M.A. Alomari, A.M. Hassan, Q.H. Al-Salami, F.Q.A. Alyousuf, M.A. Ismael, F. Alqurashi, M.A. Flayyih, Numerical analysis of Soret/Dufour MHD convection in a NEPCM-filled cavity with partial porous foam: double pipe heat exchanger application, Heat Transf. 54 (1) (2025) 788–830, https://doi.org/10.1002/htj.23185.
[51] A.M. Hassan, M.A. Alomari, A. Alajmi, A.M. Sadeq, F. Alqurashi, M.A. Flayyih, O.J. C.S.i.T.E. Kazaz, Numerical analysis of coupled fluid-structure interaction in magnetohydrodynamic flow and phase change process of nano-encapsulated phase change material systems with deformable heated surface, Case Stud. Therm. Eng. (2025) 106131, https://doi.org/10.1016/j.csite.2025.106131.
[52] D. Sáchica, E. Salcedo, C. Treviño, L. Martínez-Suástegui, Magnetohydrodynamic mixed convection and entropy generation analysis of Al2O3-water nanofluid past a confined circular cylinder, Int. J. Mech. Sci. 230 (2022) 107542, https://doi.org/10.1016/j.ijmecsci.2022.107542.
[53] P. Mondal, T.R. Mahapatra, MHD double-diffusive mixed convection and entropy generation of nanofluid in a trapezoidal cavity, Int. J. Mech. Sci. 208 (2021) 106665, https://doi.org/10.1016/j.ijmecsci.2021.106665.
[54] M. Ghalambaz, S.A.M. Mehryan, I. Zahmatkesh, A. Chamkha, Free convection heat transfer analysis of a suspension of nano–encapsulated phase change materials (NEPCMs) in an inclined porous cavity, Int. J. Therm. Sci. 157 (2020) 106503, https://doi.org/10.1016/j.ijthermalsci.2020.106503.
[55] M. Ghalambaz, M. Sabour, I. Pop, Free convection in a square cavity filled by a porous medium saturated by a nanofluid: viscous dissipation and radiation effects, engineering science and technology, int. j. 19 (3) (2016) 1244–1253.
[56] F. Selimefendigil, H.F. Öztop, Magnetohydrodynamics forced convection of nanofluid in multi-layered U-shaped vented cavity with a porous region considering wall corrugation effects, Int. Commun. Heat Mass Transf. 113 (2020) 104551, https://doi.org/10.1016/j.icheatmasstransfer.2020.104551.
[57] H. K Hamzah, F. H Ali, M. Hatami, D. Jing, Effect of two baffles on MHD natural convection in U-shape superposed by solid nanoparticle having different shapes, J. Appl. Comput. Mech. 6 (Special Issue) (2020) 1200–1209, https://doi.org/10.22055/jacm.2020.33064.2141.
[58] A.A. Pasha, M. Nayak, K. Irshad, M.M. Alam, A. Dogonchi, A.J. Chamkha, A. M. Galal, Entropy and hydrothermal analyses of nano-encapsulated phase change materials within a U-shaped enclosure: impact of diverse structures of baffles and corrugated wall, J. Energy Storage 59 (2023) 106532.
[59] M.A. Alomari, A.M. Hassan, A.M. Sadeq, F. Alqurashi, M.A.J.R.i.E. Flayyih, Double-diffusive flow and heat transfer of nano-encapsulated phase change materials in a circular cavity with partial porous region under magnetic influence, Results Eng. 26 (2025) 104646, https://doi.org/10.1016/j.rineng.2025.104646.
[60] M. Ghalambaz, A.J. Chamkha, D.J.I. j. o. h. Wen, m. transfer, Natural convective flow and heat transfer of nano-encapsulated phase change materials (NEPCMs) in a cavity, Int. J. Heat. Mass Transf. 138 (2019) 738–749, https://doi.org/10.1016/j.ijheatmasstransfer.2019.04.037.
[61] A.A. Pasha, M. Nayak, K. Irshad, M.M. Alam, A. Dogonchi, A.J. Chamkha, A.M.J.J. o.E.S. Galal, Entropy and hydrothermal analyses of nano-encapsulated phase change materials within a U-shaped enclosure: impact of diverse structures of baffles and corrugated wall, J. Energy Storage 59 (2023) 106532.
[62] S. Mehryan, M. Ismael, M. Ghalambaz, Local thermal nonequilibrium conjugate natural convection of nano-encapsulated phase change particles in a partially porous enclosure, Math. Methods Appl. Sci. (2020).
[63] M.J. Rawa, O.S. Mahdy, N.H. Abu-Hamdeh, A.J. Sultan, H. Kazemi-Varnamkhasti, S. Baghaei, M.A. Al-Ebrahim, Cooling a cavity equipped with a hot electrical element using nano-encapsulated phase change material/water: study of mixed convection and natural convection, Case Stud. Therm. Eng. 50 (2023) 103412.
[64] Usman, M., Z. Khan, M.J.P.A.S.M. Liu, and I. Applications, MHD natural convection and thermal control inside a cavity with obstacles under the radiation effects. 535 (2019) 122443.
[65] T. Kuehn, R.J.J.o.F.m. Goldstein, An experimental and theoretical study of natural convection in the annulus between horizontal concentric cylinders, J. Fluid. Mech. 74 (4) (1976) 695–719, https://doi.org/10.1017/S0022112076002012.
[66] A.M. Hassan, M.A. Alomari, A. Alajmi, A.M. Sadeq, F. Alqurashi, M.A.J.R.i. E. Flayyih, Numerical analysis of nano-encapsulated PCM magnetohydrodynamics double-diffusive convection and entropy generation in vertical enclosures with porous layer, Results Eng. 24 (2024) 103579, https://doi.org/10.1016/j.rineng.2024.103579.
[67] M.A. Alomari, A.M. Hassan, A. Alajmi, A.M. Sadeq, F. Alqurashi, M.A. Flayyih, Hydrothermal and irreversibility numerical analysis of helical coil energy storage tank with nano-encapsulated PCMs: a comprehensive study with magnetic filled, Soret/Dufour, and metallic foam effects, Appl. Therm. Eng. 266 (2025), https://doi.org/10.1016/j.applthermaleng.2025.125651.